

# Direct observation of the violation of Kirchhoff's law of thermal radiation

Received: 17 December 2022

Accepted: 25 June 2023

Published online: 24 July 2023

 Check for updates

Komron J. Shayegan<sup>1</sup>, Souvik Biswas<sup>1</sup>, Bo Zhao<sup>1</sup>, Shanhui Fan<sup>1</sup><sup>3</sup> & Harry A. Atwater<sup>1</sup>

Thermal emission—the process through which all objects with a finite temperature radiate electromagnetic energy—has generally been thought to obey reciprocity, where the absorbed and emitted radiation from a body are equal for a given wavelength and angular channel. This equality, formalized by Gustav Kirchhoff in 1860, is known as Kirchhoff's law of thermal radiation and has long guided designs to control the emitted radiation. Removing the constraint of Kirchhoff's law unlocks a multitude of applications and designs for thermal emitters. Decoupling the absorptivity and emissivity relationship can be leveraged to achieve novel functions, ranging from reducing re-emission losses to the Sun in the context of solar energy harvesting systems to radiative camouflage. Here we report the direct measurements of an inequality between the spectral directional emissivity and absorptivity for a photonic design that supports a guided-mode resonance coupled to a magneto-optic material. This inequality occurs under the application of an in-plane magnetic field that modifies the normally diagonal permittivity tensor to a non-diagonal tensor in magneto-optic InAs, resulting in an antisymmetric relationship where the magnetic tuning of enhanced emissivity for a given angle correlates with decreased absorptivity for the same angle.

Until two decades ago, thermal radiation had been considered as spatially and temporally incoherent<sup>1</sup> until narrow-linewidth, directional emissivity through grating-outcoupled surface phonon polaritons in SiC was demonstrated<sup>2</sup>. Since this initial demonstration, further work has explored the spatial and temporal coherence of thermal emission from coupled local and propagating surface phonon polaritons<sup>3,4</sup>, epsilon-near-zero (ENZ) materials<sup>5–8</sup> and photonic crystals<sup>9–12</sup>, expanding our ability to tailor thermal emission.

The major guiding principle defining both conceptual and experimental frameworks for thermal emission is the Kirchhoff's law of thermal radiation, which dictates that the absorptivity ( $\alpha$ ) and emissivity ( $e$ ) of a body at a given temperature ( $T$ ) and for a given wavelength ( $\lambda$ ), angle ( $\theta$ ) and polarization ( $\chi$ ) are equal<sup>13</sup>:

$$\alpha(\lambda, \theta, \chi, T) = e(\lambda, \theta, \chi, T) \quad (1)$$

This equality between the spectral directional absorptivity and spectral directional emissivity relies on Lorentz reciprocity<sup>14</sup>. In the case of non-reciprocal systems, a new set of laws has been developed<sup>15–17</sup>. Breaking the equality constraint on the spectral directional absorptivity and emissivity of a body is not only of fundamental importance but also has implications on exceeding current thermal radiation harvesting limits<sup>18–20</sup>. The ability to tailor absorptivity and emissivity to different values within a given channel could also enable invisible sensing or cloaking where certain wavelengths are strongly absorbed but not re-emitted back to the source<sup>21,22</sup>. Although theoretical proposals for thermal emitter configurations that break Kirchhoff's law abound<sup>23–25</sup>, experimental measurements that directly demonstrate an inequality in the absorptivity and emissivity have remained elusive.

In this work, we directly measure the absorptivity and emissivity from a non-reciprocal photonic structure and directly observe a

<sup>1</sup>Thomas J. Watson Laboratory of Applied Physics, California Institute of Technology, Pasadena, CA, USA. <sup>2</sup>Department of Mechanical Engineering, University of Houston, Houston, TX, USA. <sup>3</sup>Ginzton Laboratory and Department of Electrical Engineering, Stanford University, Stanford, CA, USA.

e-mail: [haa@caltech.edu](mailto:haa@caltech.edu)

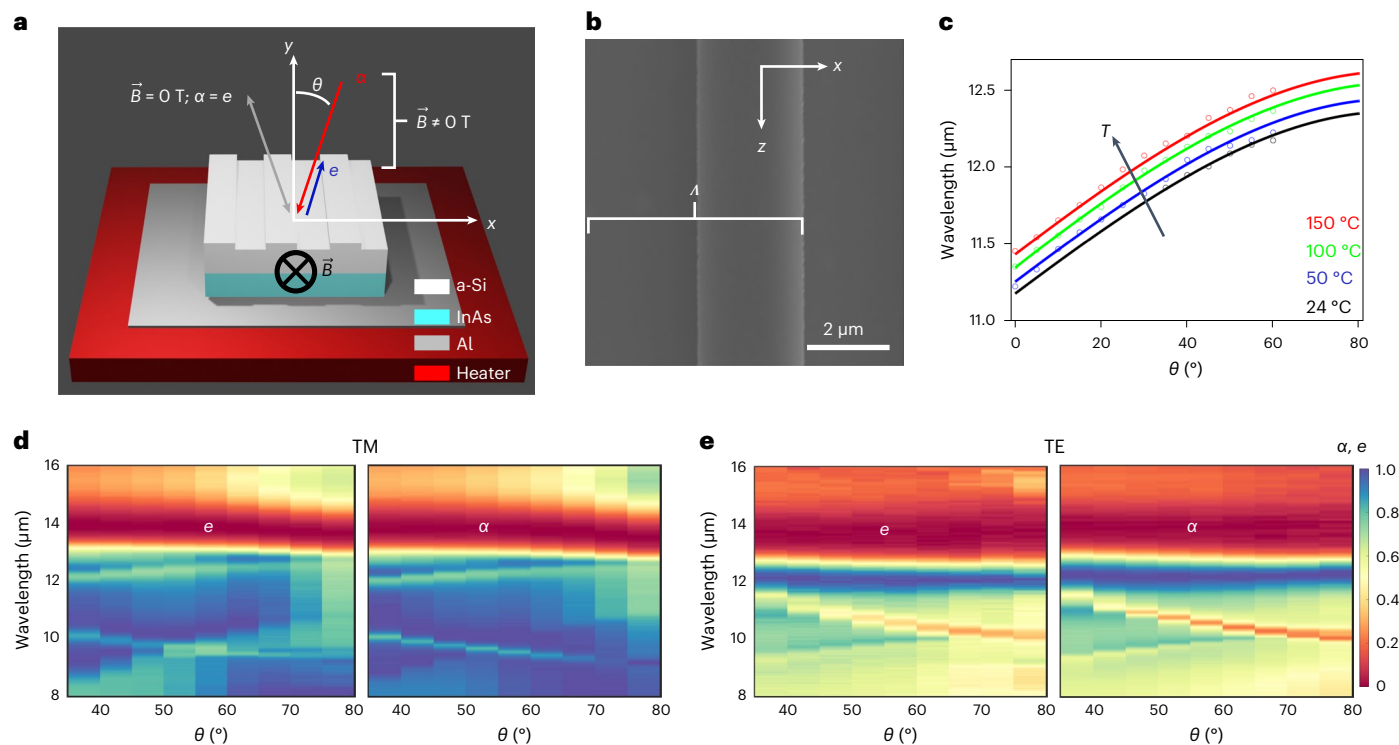


**Fig. 1 | Schematic of magnetically tunable emission and absorption of GMR structure coupled to n-InAs and comparison of zero-field absorptivity and emissivity.** **a,b**, Schematic of the GMR structure on InAs. The GMR structure has a grating periodicity  $\Lambda$  of  $5.50 \mu\text{m}$ , groove depth of  $0.50 \mu\text{m}$  and slab depth of  $1.55 \mu\text{m}$  (**a**). In the case of no applied magnetic field, the absorptivity and emissivity channels are equal (left side, grey arrow). When a transverse magnetic field is applied along the  $z$  direction, the absorptivity and emissivity (red and blue arrows, respectively) are tuned away from being equal in the same channel to being equal in opposite channels. The grating periodicity  $\Lambda$  is confirmed with scanning electron microscopy images (**b**). **c**, Experimental data (points) of

the +first-order guided-mode branch through absorptivity ( $24^\circ\text{C}$ , black) and emissivity ( $50, 100$  and  $150^\circ\text{C}$ ; blue, green and red, respectively) measurements; the curves represent theoretical calculations. The redshift in the GMR for a given  $\theta$  is a consequence of shifts in the refractive indices of a-Si and n-InAs as a function of temperature (Methods)<sup>30</sup>. **d,e**, TM-polarized (**d**) and TE-polarized (**e**) emissivity and absorptivity measurements taken at  $100^\circ\text{C}$  (left and right, respectively), showing the guided-mode dispersions. Extended Data Fig. 1 and Supplementary Fig. 1 show the full angular and spectral plots obtained through emissivity measurements for varying temperatures.

violation of Kirchhoff's law (Methods provides details of both measurements and device structure). The top layer of this photonic structure consists of a guided-mode resonance (GMR) waveguide: a dielectric slab waveguide supporting a transverse-magnetic (TM) mode that couples to free space through a grating formed on the top surface<sup>26,27</sup> (Fig. 1a,b). Such resonant structures have been used to filter and enhance infrared absorption for thermal detectors<sup>28</sup> and light trapping for solar cells<sup>29</sup>. The bottom layer consists of degenerately doped n-InAs, which has a Drude-like optical response<sup>30</sup> with a notable magnetic-field dependence near the ENZ wavelength from free-carrier contributions<sup>31</sup>. When a transverse magnetic field  $B$  is applied perpendicular to the plane of incidence (along the  $z$  axis; Fig. 1a), the permittivity tensor of the InAs develops finite off-diagonal contributions:

$$\boldsymbol{\epsilon}(\omega) = \begin{bmatrix} \epsilon_{xx} & \epsilon_{xy} & 0 \\ \epsilon_{yx} & \epsilon_{yy} & 0 \\ 0 & 0 & \epsilon_{zz} \end{bmatrix}, \quad (2)$$

$$\epsilon_{xx} = \epsilon_{yy} = \epsilon_{\infty} - \frac{\omega_p^2(\omega + i\Gamma)}{\omega[(\omega + i\Gamma)^2 - \omega_c^2]}, \quad (3)$$

$$\epsilon_{xy} = -\epsilon_{yx} = i \frac{\omega_p^2 \omega_c}{\omega[(\omega + i\Gamma)^2 - \omega_c^2]}, \quad (4)$$

$$\epsilon_{zz} = \epsilon_{\infty} - \frac{\omega_p^2}{\omega(\omega + i\Gamma)}, \quad (5)$$

where  $\omega_p = \sqrt{n e^2 / (m_e \epsilon_0)}$  and  $\omega_c = eB/m_e$  are the plasma and cyclotron frequencies, respectively;  $n = 3.0 \times 10^{18} \text{ cm}^{-3}$  is the free-carrier density;  $m_e = 0.035 m_0$  is the effective mass; and  $\Gamma = 5.1 \text{ THz}$  is the scattering rate.

This broken symmetry of the permittivity tensor results in an asymmetric angular reflection and absorption<sup>32,33</sup>. The non-reciprocal magneto-optic response is the largest when the off-diagonal contributions are the largest relative to the on-diagonal terms. Consequently, we design our structure to have strong absorption and emission features where the real part of the on-diagonal permittivity tensor crosses zero, that is, the ENZ wavelength of n-InAs.

## Results

The amorphous silicon (a-Si) GMR structure atop n-InAs is designed so that the resonance of its +first-order TM guided mode spectrally overlaps with the ENZ wavelength of n-InAs at large angles for a grating alignment of  $\phi = 0^\circ$  (Extended Data Fig. 1), where  $\phi$  is the azimuthal angle of the grating relative to the plane of incidence ( $\phi = 0^\circ$  corresponds to the grating oriented along the  $z$  axis; Fig. 1b). We choose a-Si for the GMR structure due to its low loss in the infrared compared with InAs as well as the well-developed and accessible deposition and etching techniques compared with other low-loss dielectrics like SiC. An in-depth explanation of how the periodicity and slab thickness of

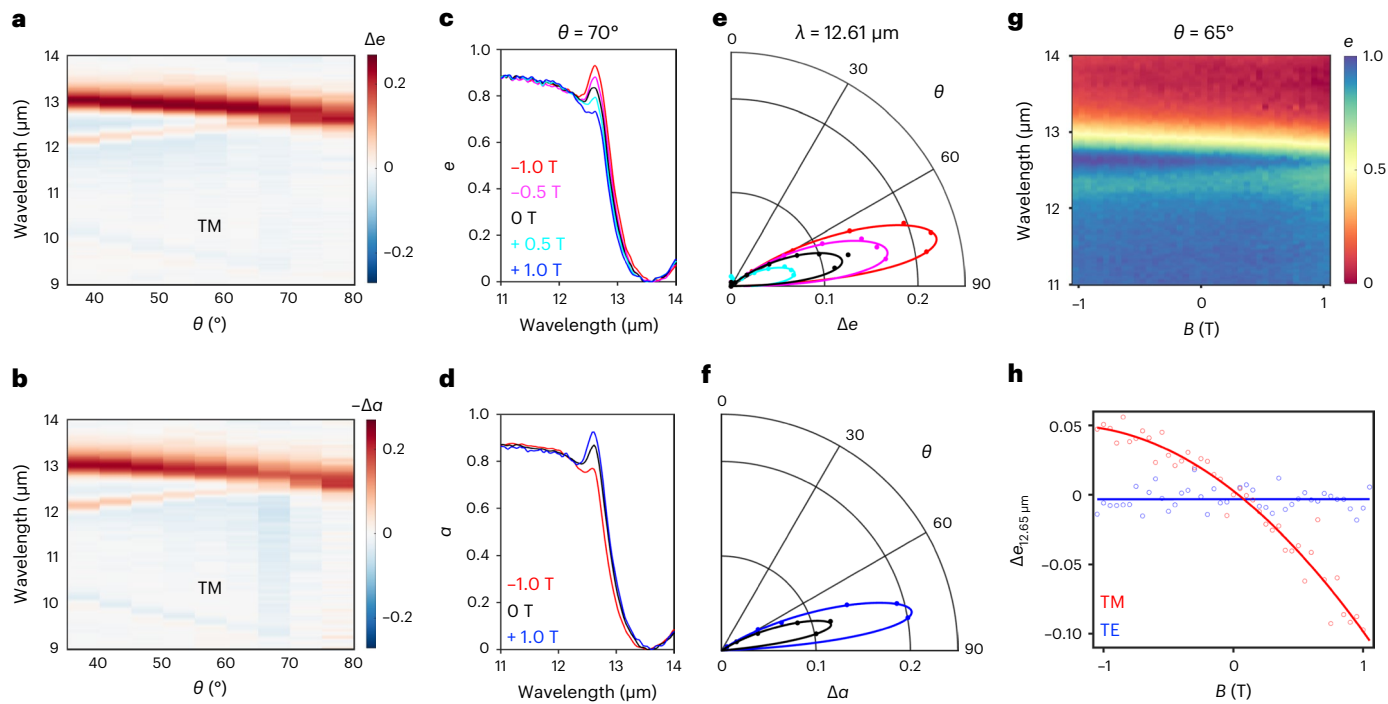


**Fig. 2 | Violation of Kirchhoff's law in absorptivity and emissivity measurements.** **a,b**, Change in the absolute emissivity and absorptivity as the applied magnetic field is switched from +1.0 to -1.0 T:  $\Delta e = e_{+1.0\text{T}} - e_{-1.0\text{T}}$  and  $\Delta \alpha = \alpha_{+1.0\text{T}} - \alpha_{-1.0\text{T}}$ . The magnetic field has an opposite effect for absorptivity and emissivity. Note that we plot  $\Delta e$  in **a** and  $-\Delta \alpha$  in **b**. **c,d**, Spectral emissivity (**c**) and absorptivity (**d**) at  $\theta = 70^\circ$  for varying magnetic fields. **e,f**, Directivity plots demonstrating the effect of the magnetic field on the resonant directional emissivity (**e**) and absorptivity (**f**) coupling through the GMR structure. We subtract the least resonant magnetic field for both emissivity and absorptivity:  $\Delta e = e - e_{-1.0\text{T}}$  and  $\Delta \alpha = \alpha - \alpha_{-1.0\text{T}}$ . Although the directionality is imposed by the GMR structure and is unchanged by the magnetic field, the outcoupling intensity is modulated by InAs. Equal and opposite tuning is observed for emissivity and

absorptivity. **g**, Measured emissivity as a function of wavelength and magnetic field for  $\theta = 65^\circ$ . The emissivity resonance is shown as the dark-blue region near  $\lambda = 12.7\text{ }\mu\text{m}$  for large negative magnetic fields. The resonant emission is tuned to a narrower linewidth and smaller amplitude with increasing magnetic field. This is a consequence of the InAs emission edge (yellow line starting at  $\lambda = 13\text{ }\mu\text{m}$  for -1 T) shifting to shorter wavelengths for increasing magnetic field. **h**, Change in emissivity near the resonance wavelength ( $\lambda = 12.65\text{ }\mu\text{m}$ ) for  $\theta = 65^\circ$  as a function of magnetic field. The TE-polarized emission shows no magnetic-field dependence, whereas the TM emissivity change is fit quadratically. This captures the beginning of the saturation effect for large negative magnetic fields. All the data were taken with the sample heated to 100 °C.

the dielectric are chosen can be found in previous work demonstrating non-reciprocal far-infrared absorption in a similar system<sup>32,33</sup>; Methods provides the fabrication details (Extended Data Figs. 2 and 3). In this work, we use a carrier concentration in n-InAs corresponding to an ENZ wavelength of 12.9 μm. By enhancing the emission at large angles with a GMR structure around this wavelength, we enable the measurement of strong emission features even at temperatures slightly above ambient conditions.

As we heat the sample above room temperature, we observe a redshift in the +first-order guided mode (Fig. 1c). At first glance, this temperature dependence seems counterintuitive, as one would naively expect a blueshift in the emission spectrum of a blackbody with increasing temperature<sup>1</sup> as well as an increase in the plasma frequency of n-InAs due to increasing carrier concentration. However, the spectral directional emissivity is determined by normalizing the collected emission of the sample by the emission from a blackbody reference; and the change in intrinsic carrier concentration in InAs over the range of temperatures (24–150 °C) is two orders of magnitude lower than the doping concentration of our sample. For doped InAs (ref. 33) and films of plasmonic materials with Drude-like optical responses<sup>34</sup>, the increase in electron–phonon scattering with temperature results in a redshift in the on-diagonal-permittivity zero-crossing wavelength. Methods provides a more in-depth discussion of the temperature-dependent spectral and angular shifts near resonance.

We plot the polarization-resolved emissivity and absorptivity measurements above room temperature next to each other (Fig. 1d,e).

Extended Data Fig. 1 shows the full angular dispersion from emissivity measurements; constraints in the absorptivity measurement setup did not allow for small angles of incidence ( $\theta < 35^\circ$ ) (Extended Data Fig. 4). The spectral directional emissivity, that is,  $e_{\text{sample}}(\lambda, \theta, \chi, T)$ , was found by subtracting the background signal and normalizing by a carbon blackbody reference emission at the same temperature, that is,  $I_{\text{Carbon BB}}(\lambda, \theta, \chi, T)$ :

$$e_{\text{sample}}(\lambda, \theta, \chi, T) = \frac{I_{\text{sample}}(\lambda, \theta, \chi, T) - I_{\text{Aluminium}}(\lambda, \theta, \chi, 24^\circ\text{C})}{I_{\text{Carbon BB}}(\lambda, \theta, \chi, T) - I_{\text{Aluminium}}(\lambda, \theta, \chi, 24^\circ\text{C})}. \quad (6)$$

The background emission intensity from the measurement apparatus was determined by measuring the emission intensity from an aluminium sample at ambient temperature, that is,  $I_{\text{Aluminium}}(24^\circ\text{C})$  (Extended Data Fig. 5)<sup>35</sup>.

Since this is a measurement in the absence of a magnetic field, the absorptivity and emissivity spectra are very similar to each other (Fig. 1d,e). The optical interference between a continuous InAs emission and spectrally sharp resonance of the guided-mode structure result in a Fano-like emissivity and absorptivity spectra. This is clear in Fig. 1d, where the +first- and -first-order guided modes are visible as lower (lighter) emissivity and absorptivity lines starting at  $\lambda = 12\text{ }\mu\text{m}$  and  $\lambda = 10\text{ }\mu\text{m}$  for  $\theta = 35^\circ$ , respectively. The resonances supported by the GMR structure have a finite bandwidth due to the intrinsic loss in

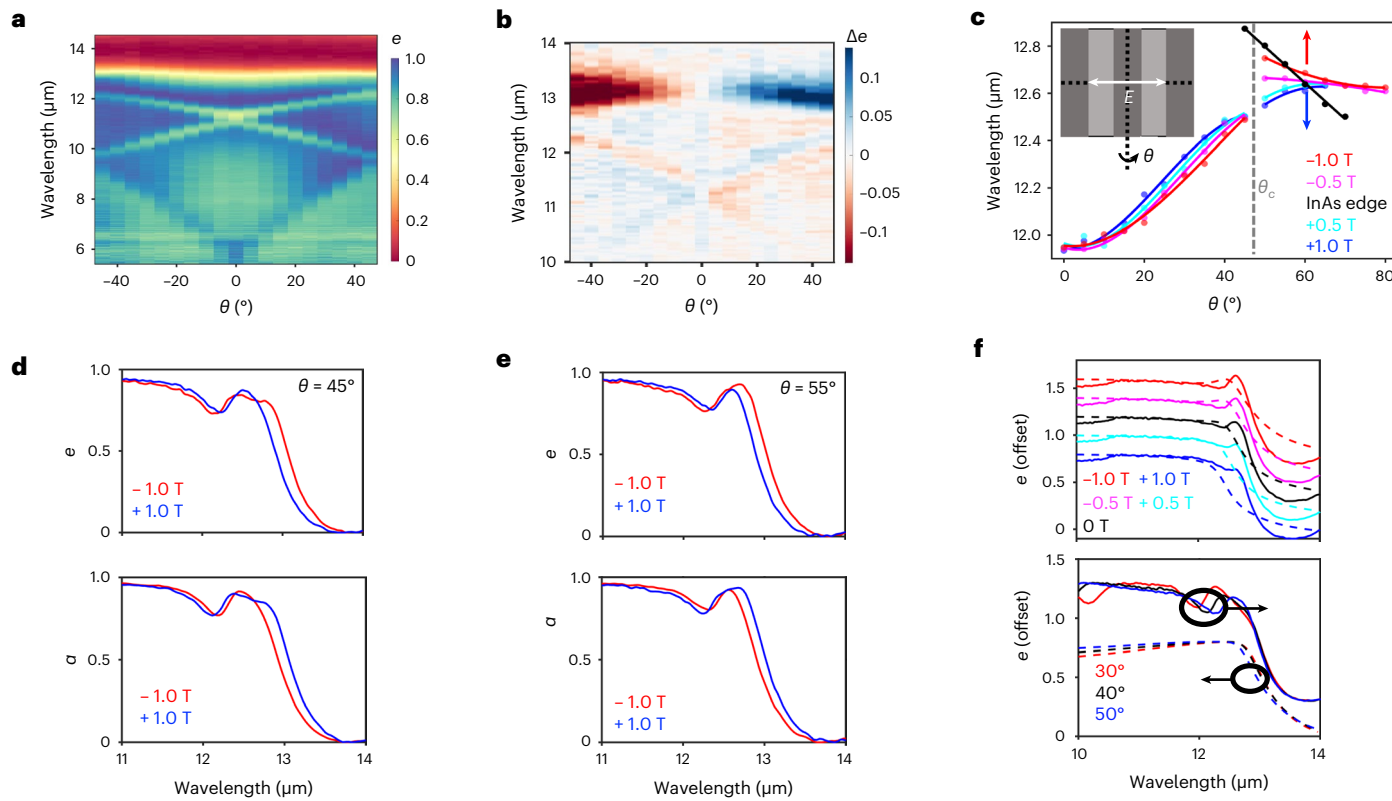


**Fig. 3 | Onsager–Casimir relations for emissivity and absorptivity in a magnetic field.** **a**, TM emissivity measurements for zero applied magnetic field when the outgoing angle is near normal incidence. The +first- and −first-order guided-mode branches are visible from 10 to 12 μm as lighter features. **b**, Change in emissivity from −1.0 to +1.0 T across normal incidence. The antisymmetric (across  $\theta = 0^\circ$ ) shifts in intensity associated with the guided-mode peaks are visible as light blue and red features from 10 to 12 μm. The Brewster mode of InAs is visible from 13.0 to 13.5 μm as the blue and red strips. Note that because of measurement constraints, we cannot access the angles where the GMR and Brewster mode overlap. **c**, TM emissivity maxima for varying magnetic fields. The maxima follow the GMR and are strongly tuned for large angles ( $\theta > \theta_c \approx 50^\circ$ ), where the InAs emission edge overlaps with the resonance. **d,e**, Emissivity and

absorptivity spectra above (d) and below (e)  $\theta_c = 50^\circ$ . For  $\theta = 45^\circ$ , the spectral shift in peak emissivity does not align with the InAs shift; however, for  $\theta = 50^\circ$ , the peak shift aligns with the magnetic-field shift in InAs. Opposite magnetic field effects are observed for absorptivity and emissivity. **f**, Emissivity measurements of the photonic structure (solid) and simulations of InAs emissivity (dashed) for  $\theta = 70^\circ$  for varying magnetic fields (top). The blueshift in the InAs emission edge for a positive field results in smaller emissivity. Conversely, a redshift in the InAs emission edge for negative fields results in larger emissivity. Emissivity measurements of the photonic structure (solid) and simulations of the InAs emissivity (dashed), illustrating the opposite spectral shift in GMR and InAs emission edge as a function of  $\theta$  for zero applied magnetic field (bottom). All the data were taken with the sample heated to 100 °C.

the system<sup>36,37</sup>. We are able to qualitatively capture this in COMSOL simulations (Supplementary Fig. 1).

The low emissivity and absorptivity band for  $\lambda > 13 \mu\text{m}$  for both TM-polarized and transverse-electric (TE)-polarized light (Fig. 1d,e) is due to the low absorption/emission from n-InAs at wavelengths longer than the plasma wavelength. We refer to this transition from high to low emissivity of n-InAs across all the angles as the InAs emissivity edge.

By turning on a transverse, reciprocity-breaking magnetic field, we demonstrate a direct violation of Kirchhoff's law (Fig. 2). In Fig. 2a,b, we compare the change in emissivity and absorptivity for two opposite-valued magnetic fields, that is, −1 and +1 T. We observe that the change in absorptivity  $\Delta\alpha = \alpha_{-1.0 \text{ T}} - \alpha_{1.0 \text{ T}}$  is opposite in sign to the observed change in emissivity  $\Delta e = e_{-1.0 \text{ T}} - e_{1.0 \text{ T}}$ . Note that  $\Delta e \cong -\Delta\alpha$  over the full spectral and angular range. Figure 2a,b also highlights the two spectral features at play: the InAs emissivity/absorptivity edge (red line starting at  $\lambda \cong 13 \mu\text{m}$  and  $\theta = 35^\circ$ ) and the +first-order GMR from the a-Si structure (faint red line starting at  $\lambda \cong 12 \mu\text{m}$  and  $\theta = 35^\circ$ ). The two features intersect near  $\theta = 65^\circ$ , resulting in resonance tuning with the magnetic field. Tuning of the peak-emissivity spectral position, however, onsets at a smaller, critical angle ( $\theta_c = 50^\circ$ ). This is a consequence of the InAs emission edge pulling the +first-order GMR emissivity peak even when both are not fully spectrally overlapped. This is discussed in depth later in the Article with reference to Fig. 3c.

To achieve a more quantitative view of the magnetic-field tuning when Kirchhoff's law is broken, we display the emissivity and absorptivity at a specific angle of  $\theta = 70^\circ$  (Fig. 2c,d). For both emissivity and absorptivity, we observe that the GMR coupled to InAs is strongly affected by the transverse magnetic field. From a theoretical viewpoint, in the absence of other diffraction channels, this magnetic tuning having an opposite effect on the absorptivity and emissivity at a given angle derives from the Onsager–Casimir relations<sup>38</sup> for an absorber in an external magnetic field  $B$ :

$$\alpha(\lambda, -\theta, B) = \alpha(\lambda, \theta, -B), e(\lambda, -\theta, B) = e(\lambda, \theta, -B). \quad (7)$$

In other words, swapping the positions of the source and detector ( $\theta \rightarrow -\theta$ ) has the same effect as changing the sign of the reciprocity-breaking external field ( $B \rightarrow -B$ ). To test this relationship, we rotate the sample stage to measure the sample emission for  $-\theta$  and  $+\theta$  and  $-B$  and  $+B$  (our experimental setup does not allow the measurements of absorptivity around normal incidence). With zero magnetic field, the emission of the photonic structure is symmetric across  $\theta = 0^\circ$ :  $e(\lambda, \theta) = e(\lambda, -\theta)$  (Fig. 3a). For non-zero magnetic field, we display the change in emissivity,  $\Delta e = e_{-1.0 \text{ T}} - e_{1.0 \text{ T}}$ , and observe equal and opposite effects of the magnetic field across  $\theta = 0^\circ$  (Fig. 3b).

Equation (7) has been further developed in the context of a non-reciprocal absorber/emitter with a transverse magnetic field<sup>16,17</sup>. Because our structure exhibits a compound symmetry that combines a mirror operator with an operator that flips the sign of the magnetic field, the spectral directional absorptivity and emissivity are related by<sup>17</sup>

$$\alpha(\lambda, -\theta, B) = e(\lambda, \theta, B). \quad (8)$$

Taking the right-hand-sides of equations (7) and (8), we note that  $\alpha(\lambda, \theta, -B) = e(\lambda, \theta, B)$ . The opposite  $B$ -field dependence for emissivity and absorptivity is apparent from our measurements (Figs. 2a–f and 3d,e). To illustrate this, in Fig. 2e,f, we show directivity profiles at the resonant wavelength by subtracting the largest positive-magnetic-field emissivity spectrum at each angle (largest negative-magnetic-field spectrum at each angle for absorptivity), from the spectra for the other applied magnetic fields. We observe that the directionality of emissivity and absorptivity at the resonant wavelength does not change by varying the magnetic field. Although the magnitude of emissivity and absorptivity is modulated, the angular profile remains unchanged. This can be understood from the fact that the directionality of thermal emission is imposed by the grating structure, which does not have a dependence on the magnetic field.

We also vary the magnetic field at a single angle ( $\theta = 65^\circ$ ) in a fine sweep and measure the emissivity from the structure (Fig. 2g). At a large negative magnetic field, the resonant emission is both large in amplitude and broad in linewidth (from 12.5 to 12.8  $\mu\text{m}$ ; Fig. 2g, dark-blue region). As the magnetic field is increased to positive values, the InAs emission edge (yellow line starting at 13  $\mu\text{m}$  for  $-1\text{ T}$ ; Fig. 2g) blueshifts and reduces both amplitude and linewidth of the resonant emission. Methods provides a detailed discussion of the InAs emission edge shifting and the resonant emission amplitude decreasing with the increasing magnetic field (Extended Data Fig. 6).

Figure 2h shows the magnetic-field-dependent change in the emissivity at  $\lambda = 12.65\text{ }\mu\text{m}$  (near the resonant wavelength) relative to the zero-field case for both TM- and TE-polarized thermal emissions. For the TE-polarized emission, as expected, we observe no modulation of emissivity. For TM-polarized light, the change in emissivity for a positive magnetic field is approximately linear ( $-0.1/T$ ). This approximately linear magnetic-field dependence of the emissivity and absorptivity for positive fields is expected from the cyclotron resonance of InAs (ref. 39). Methods provides details of this linear regime.

However, over the full magnetic-field range ( $-1$  to  $+1\text{ T}$ ; Fig. 2h), we fit the change in emissivity to a quadratic function. At large negative magnetic fields, the emissivity modulation decreases. This is because the upper and lower bounds of the emissivity of the photonic structure are dominated by the emissivity of n-InAs. The saturation of emissivity tuning for increased emissivity (negative magnetic field) is a consequence of the fact that the spectral radiance cannot exceed that of the emitted blackbody spectrum (that is, cannot become super-Planckian)<sup>40</sup>. This is confirmed both in simulation (Extended Data Fig. 7 and Supplementary Fig. 3) and in a further analysis of the experimental data (Extended Data Fig. 6).

By mapping the emissivity maxima for the +first-order guided mode over the full angular range, we can visualize the wavelength and amplitude tuning of both emissivity and absorptivity with magnetic field (Fig. 3c). The magnetic-field-induced shifts in the emissivity and absorptivity resonance amplitude and, to a lesser extent, the resonant wavelength shifts, are due to the shift in the InAs emissivity edge.

We observe a large modulation of the resonant emissivity amplitude for large angles (Fig. 2c and Extended Data Fig. 8c). In this range, ( $\theta > 65^\circ$ ), the emissivity of the device is non-resonant for the positive-field cases and no maxima larger than the InAs background are found (Extended Data Fig. 8c), represented by the absence of blue markers for the emissivity maxima in Fig. 3c. For  $e(\lambda, 70^\circ, +1.0\text{ T})$

or  $\alpha(\lambda, 70^\circ, -1.0\text{ T})$ , the emission wavelength of the InAs blueshifts (Fig. 3f (top), dashed blue trace) and no longer strongly outcouples through the GMR structure (Fig. 3f (top), solid blue trace). For  $e(\lambda, 70^\circ, -1.0\text{ T})$ , the magnetic field shifts the emission wavelength of InAs to longer values compared with the zero-field case, resulting in stronger resonance and outcoupling through the GMR structure and into the far field (Fig. 3f (top), red trace).

Tuning of the emissivity and absorptivity resonance wavelength is the strongest near a critical incidence angle ( $\theta_c \approx 50^\circ$ ; Fig. 3c). As shown in Fig. 3f (bottom), for increasing  $\theta$ , the +first-order guided mode redshifts (solid traces) and the InAs emission wavelength blueshifts (dashed traces). Near  $\theta_c = 50^\circ$ , the InAs emission wavelength and +first-order GMR begin to spectrally overlap. For sufficiently large negative fields, the InAs emissivity has its own peak known as the Brewster mode<sup>41</sup> (Fig. 3f (top), red trace), which—when sufficiently spectrally overlapped with the GMR—pulls the overall peak emissivity to longer wavelengths (Fig. 3e and Extended Data Fig. 8b). Below  $\theta_c$ , the spectral overlap between the InAs emission wavelength and +first-order GMR is mismatched enough that the wavelength of the emissivity peak is dominated by the GMR (Fig. 3d and Extended Data Fig. 8a). The same is true for absorptivity; however, the role of the magnetic field is reversed (Fig. 3d,e).

In summary, we measured the emissivity and absorptivity of a magneto-optic photonic structure, giving direct experimental evidence for the violation of Kirchhoff's law of thermal radiation under a modest transverse magnetic field. We find that the dependence of absorptivity and emissivity detuning for small applied magnetic fields is linearly dependent on the magnetic field; however, it saturates when the peak emissivity approaches 1. Both spectral and directional tunings of the emissivity and absorptivity are described by the Onsager-Casimir relations. These results open the path for future experimental work on Kirchhoff-violating thermal emitters. Owing to the ubiquity of devices and applications for both non-reciprocal photonics and thermal emitters, numerous theoretical works have proposed combining these two concepts to address phenomena related to radiative cooling<sup>42</sup>, solar energy harvesting<sup>43</sup> and spin-polarized light sources<sup>16</sup>. Our work demonstrates the decoupling of absorptivity and emissivity for such devices, and opens the door to more complex designs that realize distinct emissivity and absorptivity channels<sup>44</sup>. The non-reciprocal mechanism in this work, a strong gyrotropic effect around the ENZ wavelength of n-InAs, can be extended to implement the Kirchhoff violation over a broadband spectral range<sup>45</sup>. Alternative materials<sup>46</sup> can also be used to reduce, or even remove<sup>47</sup>, the requirement of an external magnetic field. Beyond materials with an inherent non-reciprocal optical response, methods of implementing non-reciprocal devices using spatiotemporal modulation<sup>48</sup> or other external, unidirectional biasing<sup>49</sup> are avenues towards other Kirchhoff-violating emitters.

## Online content

Any methods, additional references, Nature Portfolio reporting summaries, source data, extended data, supplementary information, acknowledgements, peer review information; details of author contributions and competing interests; and statements of data and code availability are available at <https://doi.org/10.1038/s41566-023-01261-6>.

## References

1. Planck, M. *The Theory of Heat Radiation* (Forgotten Books, 2013).
2. Greffet, J.-J. et al. Coherent emission of light by thermal sources. *Nature* **416**, 61–64 (2002).
3. Lu, G. et al. Engineering the spectral and spatial dispersion of thermal emission via polariton-phonon strong coupling. *Nano Lett.* **21**, 1831–1838 (2021).
4. Caldwell, J. D. et al. Low-loss, extreme subdiffraction photon confinement via silicon carbide localized surface phonon polariton resonators. *Nano Lett.* **13**, 3690–3697 (2013).

5. Jun, Y. C., Lik, T. S. & Ellis, A. R. Doping-tunable thermal emission from plasmon polaritons in semiconductor epsilon-near-zero thin films. *Appl. Phys. Lett.* **105**, 131109 (2014).
6. Xu, J., Mandal, J. & Raman, A. P. Broadband directional control of thermal emission. *Science* **372**, 393–397 (2021).
7. Park, J. et al. Dynamic thermal emission control with InAs-based plasmonic metasurfaces. *Sci. Adv.* **4**, eaat3163 (2018).
8. Liberal, I. & Engheta, N. Near-zero refractive index photonics. *Nat. Photon.* **11**, 149–158 (2017).
9. Luo, C., Narayanaswamy, A., Chen, G. & Joannopoulos, J. D. Thermal radiation from photonic crystals: a direct calculation. *Phys. Rev. Lett.* **93**, 2113905 (2004).
10. De Zoysa, M. et al. Conversion of broadband to narrowband thermal emission through energy recycling. *Nat. Photon.* **6**, 535–539 (2012).
11. Baranov, D. G. et al. Nanophotonic engineering of far-field thermal emitters. *Nat. Mater.* **18**, 920–930 (2019).
12. Laroche, M., Carminati, R. & Greffet, J.-J. Coherent thermal antenna using a photonic crystal slab. *Phys. Rev. Lett.* **96**, 123903 (2006).
13. Kirchhoff, G. On the relationship between the emissivity and absorptivity of a body for heat and light. *Ann. Phys.* **109**, 275–301 (1860).
14. Lorentz, H. A. The theorem of Poynting concerning the energy in the electromagnetic field and two general propositions concerning the propagation of light. *Verl. K. Akad. W Amsterdam* **4**, 176 (1896).
15. Miller, D. A. B., Zhu, L. & Fan, S. Universal modal radiation laws for all thermal emitters. *Proc. Natl Acad. Sci. USA* **114**, 4336–4341 (2017).
16. Khandekar, C., Khosravi, F., Li, Z. & Jacob, Z. New spin-resolved thermal radiation laws for nonreciprocal bianisotropic media. *New J. Phys.* **22**, 123005 (2020).
17. Guo, C., Zhao, B. & Fan, S. Adjoint Kirchhoff's law and general symmetry implications for all thermal emitters. *Phys. Rev. X* **12**, 021023 (2022).
18. Green, M. A. Time-asymmetric photovoltaics. *Nano Lett.* **12**, 5985–5988 (2012).
19. Fan, S. Thermal photonics and energy applications. *Joule* **1**, 264–273 (2017).
20. Buddhiraju, S., Santhanam, P. & Fan, S. Thermodynamic limits of energy harvesting from outgoing thermal radiation. *Proc. Natl Acad. Sci. USA* **115**, 3609–3615 (2018).
21. Huang, R., Miranowicz, A., Liao, J.-Q., Nori, F. & Jing, H. Nonreciprocal photon blockade. *Phys. Rev. Lett.* **121**, 153601 (2018).
22. Sounas, D. L. & Alù, A. Non-reciprocal photonics based on time modulation. *Nat. Photon.* **11**, 774–783 (2017).
23. Zhu, L. & Fan, S. Near-complete violation of detailed balance in thermal radiation. *Phys. Rev. B* **90**, 220301 (2014).
24. Zhao, B., Guo, C., Garcia, C. A., Narang, P. & Fan, S. Axion-field-enabled nonreciprocal thermal radiation in Weyl semimetals. *Nano Lett.* **20**, 1923–1927 (2020).
25. Pajovic, S., Tsurimaki, Y., Qian, X. & Chen, G. Intrinsic nonreciprocal reflection and violation of Kirchhoff's law of thermal radiation in planar type-I magnetic Weyl semimetal surfaces. *Phys. Rev. B* **102**, 165417 (2020).
26. Wang, S. S., Magnusson, R., Bagby, J. S. & Moharam, M. G. Guided-mode resonances in planar dielectric-layer diffraction gratings. *J. Opt. Soc. Am.* **7**, 1470–1474 (1990).
27. Fattal, D., Li, J., Peng, Z., Fiorentino, M. & Beausoleil, R. G. Flat dielectric grating reflectors with focusing abilities. *Nat. Photon.* **4**, 466–470 (2010).
28. Kamboj, A. et al. All-epitaxial guided-mode resonance mid-wave infrared detectors. *Appl. Phys. Lett.* **118**, 201102 (2021).
29. Khaleque, T. & Magnusson, R. Light management through guided-mode resonances in thin-film silicon solar cells. *J. Nanophoton.* **8**, 083995 (2014).
30. Paskov, P. P. Refractive indices of InSb, InAs, GaSb, InAs<sub>x</sub>Sb<sub>1-x</sub>, and In<sub>1-x</sub>Ga<sub>x</sub>Sb: effects of free carriers. *J. Appl. Phys.* **91**, 1890 (1997).
31. Heyman, J. N. et al. Terahertz emission from GaAs and InAs in a magnetic field. *Phys. Rev. B* **64**, 085202 (2001).
32. Liu, M. et al. Nonreciprocal thermal radiation in ultrathin magnetized epsilon-near-zero semiconductors. Preprint at <https://arxiv.org/abs/2203.04488> (2022).
33. Shayegan, K. J., Zhao, B., Kim, Y., Fan, S. & Atwater, H. A. Nonreciprocal infrared absorption via resonant magneto-optical coupling to InAs. *Sci. Adv.* **8**, eabm4308 (2022).
34. Reddy, H. et al. Temperature-dependent optical properties of plasmonic titanium nitride thin films. *ACS Photonics* **4**, 1413–1420 (2017).
35. Boyd, R. W. *Radiometry and The Detection of Optical Radiation* (Wiley, 1983).
36. Lalanne, P. et al. Quasinormal mode solvers for resonators with dispersive materials. *J. Opt. Soc. Am. A* **36**, 686–704 (2019).
37. Li, J., Li, Z. & Shen, S. Degenerate quasi-normal mode theory for near-field radiation between plasmonic structures. *Opt. Express* **28**, 34123–34136 (2020).
38. Casimir, H. B. G. On Onsager's principle of microscopic reversibility. *Rev. Mod. Phys.* **17**, 350 (1945).
39. Zhao, B. et al. Near-complete violation of Kirchhoff's law of thermal radiation with a 0.3 T magnetic field. *Opt. Lett.* **44**, 4204 (2019).
40. Xiao, Y., Sheldon, M. & Khats, M. A. Super-Planckian emission cannot really be 'thermal'. *Nat. Photon.* **16**, 397–401 (2022).
41. Taliercio, T., Guilengui, V. N., Cerutti, L., Tournié, E. & Greffet, J.-J. Brewster 'mode' in highly doped semiconductor layers: an all-optical technique to monitor doping concentration. *Opt. Express* **22**, 24294–24303 (2014).
42. Fan, S. & Li, W. Photonics and thermodynamics concepts in radiative cooling. *Nat. Photon.* **12**, 182–190 (2022).
43. Park, Y., Zhao, B. & Fan, S. Reaching the ultimate efficiency of solar energy harvesting with a nonreciprocal multijunction solar cell. *Nano Lett.* **22**, 448–452 (2022).
44. Zhao, B. et al. Nonreciprocal thermal emitters using metasurfaces with multiple diffraction channels. *Phys. Rev. Applied* **16**, 064001 (2021).
45. Hwang, J. S., Xu, J. & Raman, A. Simultaneous control of spectral and directional emissivity with gradient epsilon-near-zero InAs photonic structures. Preprint at <https://arxiv.org/abs/2212.14112> (2022).
46. Zhang, Z. & Zhu, L. Broadband nonreciprocal thermal radiation. *Phys. Rev. Applied* **19**, 014013 (2023).
47. Liu, E. et al. Giant anomalous Hall effect in a ferromagnetic kagome-lattice semimetal. *Nat. Phys.* **14**, 1125–1131 (2018).
48. Hadad, Y., Soric, J. C. & Alù, A. Breaking temporal symmetries for emission and absorption. *Proc. Natl Acad. Sci. USA* **113**, 3471–3475 (2016).
49. Gangaraj, S. A. H. & Monticone, F. Drifting electrons: nonreciprocal plasmonics and thermal photonics. *ACS Photonics* **9**, 806–819 (2022).
50. Bergmann, J., Heusinger, M., Andrä, G. & Falk, F. Temperature dependent optical properties of amorphous silicon for diode laser crystallization. *Opt. Express* **20**, A856–A863 (2012).

**Publisher's note** Springer Nature remains neutral with regard to jurisdictional claims in published maps and institutional affiliations.

Springer Nature or its licensor (e.g. a society or other partner) holds exclusive rights to this article under a publishing agreement with the author(s) or other rightsholder(s); author self-archiving of the accepted manuscript version of this article is solely governed by the terms of such publishing agreement and applicable law.

© The Author(s), under exclusive licence to Springer Nature Limited 2023

## Methods

### Temperature-dependent optical properties of n-InAs and a-Si

To carry out emissivity measurements in ambient conditions, we first need an understanding of the temperature dependence of the optical properties of the constituent layers of our photonic structure. We do this via spectroscopic ellipsometry, where a parameterized fit of the amplitude and phase of the ratio of the reflected *p*- and *s*-polarized light is used to model the refractive index of the sample.

We first measure the *p*- and *s*-polarized reflectance of the n-InAs wafer at 50, 100 and 150 °C and use a Drude model to extract the infrared refractive index (Extended Data Fig. 1a). After building a model that captures the shift in the refractive index of n-InAs at the given temperatures, we deposit a 2-μm-thick layer of a-Si on the wafer and measure the refractive index again at the same set of temperatures. This is again done via spectroscopic ellipsometry; however, we reuse the models for bare InAs so that we are only fitting for the deposited a-Si layer at the given temperatures.

We observe an increase in the refractive index of the a-Si layer as a function of temperature (Extended Data Fig. 1b). This shift can also be seen in our emissivity measurements, where the GMR redshifts with increasing temperature (Fig. 1c).

Solving a toy model of the +first-order guided-mode branch, which incorporates the refractive index of the a-Si for the upper and lower bounds of the resonance condition<sup>26</sup>, we get

$$\gamma n_{\text{a-Si}} - \Delta \leq n_{\text{air}} \sin(\theta) - m \frac{\lambda}{\beta \Lambda} < \gamma n_{\text{a-Si}}, \quad (9)$$

where  $\gamma$  and  $\beta$  are the scaling coefficients held constant over all the temperatures,  $n_{\text{a-Si}}$  is the refractive index of the a-Si layer,  $\Delta$  is the average perturbation of the refractive index due to the presence of grating,  $n_{\text{air}}$  is the refractive index of air,  $\theta$  is the incident angle,  $m$  is the diffractive order and  $\Lambda$  is the periodicity of the grating. Using the different refractive indices of  $n_{\text{a-Si}}$  at three different temperatures, we track the GMR of our device for different temperatures (Extended Data Fig. 1c–e).

### GMR structure fabrication and modelling

Extended Data Fig. 2 outlines the fabrication process of the GMR structure. We start by cleaning the n-InAs wafer in a sonicated acetone bath, followed by a sonicated isopropyl alcohol bath. Following the cleaning process, we deposit 2.05 μm of a-Si using plasma-enhanced chemical vapour deposition at 200 °C at a gas flow rate of 250 s.c.c.m. (5% SiH<sub>4</sub>/95% argon balance).

The next step requires etching gratings into the a-Si layer. To do this, we spin on a 750-nm-thick layer of ZEP520A and write the grating pattern into the resist with an electron-beam pattern generator. After developing the resist in ZED-N50 and rinsing the sample in isopropyl alcohol, we bake the sample for 4 min at 150 °C to create a hard mask for the etching process. To etch away 0.5 μm of the a-Si layer, we use an inductively coupled plasma-reactive ion etcher with a pseudo-Bosch process (SF<sub>6</sub> and C<sub>4</sub>F<sub>8</sub> gases).

Once the pattern is confirmed using an optical microscope, we leave the sample in Remover PG overnight and rinse the final sample in isopropyl alcohol and deionized water. We take scanning electron microscopy images of the final grating (Extended Data Fig. 3b) as well as the thickness of a-Si deposited on InAs (Extended Data Fig. 3a) to fine-tune the deposition and etching process.

### Emissivity and absorptivity measurement techniques and fitting

We use two different systems to directly measure the emissivity and absorptivity. The emissivity measurement system is a home-built, angle-resolved, thermal emission spectroscopy setup<sup>51</sup>. The sample is mounted at the rotation axis of a goniometer (Thorlabs BGM12CC) with an angular range of ±45°. The goniometer itself is on a 45° wedge

so that we collect over an emission angular range of 0–90°. The rotation axis is positioned between the faces of the pole pieces of a low-field electromagnet (GMW 5403). The field strength across the gap between the pole pieces is measured using a Hall sensor (Lake Shore HGT-1010) and is found to be uniform across the sample. The field strength can be tuned by changing the current through the electromagnet coils or changing the pole gap. For our experiments, we keep the pole gap constant at 15 mm.

The areas of the carbon blackbody and the sample are the same (7 mm × 7 mm). We collect the emission from the sample with a ZnSe lens and pass the light into a Fourier-transform infrared spectrometer. We align both sample surfaces to the focus of the ZnSe lens (spot size, ~100 μm) using the internal alignment laser of the spectrometer. For polarization-resolved measurements, we place a wire-grid polarizer in front of a deuterated lanthanum triglycine sulfate detector (Extended Data Fig. 4a).

To enhance the signal-to-noise ratio, we heat the sample with a small-form resistive heater above room temperature (50, 100 and 150 °C). A temperature-stable polyimide tape is used to fix the sample to the resistive heater. We subtract the room-temperature signal by repeating the same measurements of aluminium at room temperature. The intensity of the sample signal is then normalized by a carbon blackbody prepared by spraying a solution of carbon black onto carbon paper (Sigracet 38 BC) (Extended Data Fig. 5). Carbon black samples were also made by coating a silicon wafer with carbon black; however, the non-uniformity of the carbon black distribution made it less desirable for normalization purposes.

The absorptivity measurements were done using a J.A. Woollam infrared ellipsometer in the reflection-transmission mode. All the absorptivity measurements were normalized against a gold reference sample with the same area as the device to account for the shape of the infrared spot changing as a function of angle. Because the source and detector are housed in large compartments, we were limited to incidence angles above 35°. Instead of an electromagnet, we used a Halbach array<sup>52</sup> to apply the transverse magnetic field in the absorptivity setup. The field strengths could be tuned by changing the pole gap (Extended Data Fig. 4b).

Out of the two measurement systems, the spectral bandwidth of the emissivity measurement setup limits the full spectral range available. This is because the polarizer and ZnSe lens have non-uniform transmission outside of the 7–16 μm range. To keep the data analysis consistent across both measurements, we worked with normalized data from 8 to 16 μm for both absorptivity and emissivity measurements. This yielded consistent matching of the spectra across the two measurement setups for the zero-magnetic-field case.

For a deeper analysis of the experimental measurements, we fit the fine magnetic-field sweep data taken at θ = 65° (Fig. 2g). We break the contributions to the emissivity of the photonic structure into two components: a sigmoid, representing the InAs emission edge, and a Fano-like resonance that results from the GMR aligned to the InAs emission edge (Extended Data Fig. 6a). When these two components are combined, the wavelength shift in the emission is due to a blueshift in the InAs emission edge for a positive magnetic field and redshift for a negative magnetic field (Extended Data Fig. 6b). This spectral shift in the InAs emission edge is linear as a function of magnetic field (Extended Data Fig. 6c). The Fano-like resonance produces a small change in the central wavelength for varying magnetic fields (Extended Data Fig. 6d), and its most notable magnetic-field response is the reduction in the resonant amplitude (Extended Data Fig. 6e).

An interesting point to note is that the emissivity tuning of the photonic structure saturates for a sufficiently large magnetic field at a given wavelength (Fig. 2h). This linear behaviour in the shift in the sigmoid central wavelength is reflected when looking at the average change in the emissivity of the photonic structure over a wavelength range that

spans the emission edge (Supplementary Figs. 3c,d and 5). However, for a single wavelength that corresponds to the maximum emissivity of the structure under a negative magnetic field ( $\lambda = 12.65 \mu\text{m}$ ; Extended Data Fig. 6a, red trace), the emissivity tuning saturates because of the constraint of Planckian emission (that is, the sample emissivity cannot exceed 1). This effect is only discernible when the emissivity approaches 1. We replot Fig. 2h next to simulations for the same angle ( $\theta = 65^\circ$ ) and at the simulation resonant wavelength under a negative magnetic field ( $\lambda = 12.65 \mu\text{m}$ ) (Extended Data Fig. 7). At lower emissivity, the magnetic tuning of the emissivity appears linear.

Beyond the fine sweep of the magnetic field at  $\theta = 65^\circ$ , we can also understand the mechanisms of emissivity and absorptivity tuning by looking at the emissivity spectra for three different characteristic angular ranges:

- I. Completely uncoupled: where the magneto-optic shift in the InAs emission edge is spectrally mismatched from the +first-order GMR ( $0^\circ < \theta < 45^\circ$ ). Extended Data Fig. 8a shows this for  $\theta = 25^\circ$ . The spectral position of the peak emissivity is not discernibly affected by the magneto-optic shift in InAs.
- II. ‘Mode pulling’: where the InAs emission edge and +first-order GMR are slightly spectrally mismatched, resulting in peak emissivity switching between the GMR and Brewster mode depending on the magnetic-field sign ( $\theta = 50^\circ, 55^\circ$ ). Extended Data Fig. 8b shows this for  $\theta = 55^\circ$ . The spectral position of the peak emissivity is ‘pulled’ blue (for a positive magnetic field) and red (for a negative magnetic field) by the magneto-optic shift in InAs.
- III. Completely coupled: where the InAs emission edge is completely spectrally overlapped with the +first-order GMR ( $\theta > 60^\circ$ ). Extended Data Fig. 8c shows this for  $\theta = 70^\circ$ . The spectral position of peak emissivity does not move; however, the magneto-optic shift in InAs tunes the emissivity to being above (negative field) and below (positive field) the emissivity background.

## Data availability

The data that support the plots within this paper and other findings of this study are available from the corresponding author upon reasonable request.

## References

51. Zhong, F. et al. Angle-resolved thermal emission spectroscopy characterization of non-Hermitian metacrystals. *Phys. Rev. Applied* **13**, 014071 (2020).
52. Adambukulam, C. et al. An ultra-stable 1.5 tesla permanent magnet assembly for qubit experiments at cryogenic temperatures. *Rev. Sci. Instrum.* **92**, 085106 (2021).

## Acknowledgements

We acknowledge discussions with A. Laucht and D. H. Drew. This work has been supported by DARPA NLM (grant no. HR00111820046). K.J.S. acknowledges support from the NSF for a graduate research fellowship.

## Author contributions

H.A.A. and S.F. conceived the project. K.J.S. fabricated the samples and carried out the measurements, supported by S.B. K.J.S. led the data analysis and modelling, with support from S.B. and B.Z. H.A.A. supervised the project. K.J.S., S.B. and H.A.A. wrote the manuscript with input from all other authors.

## Competing interests

The authors declare no competing interests.

## Additional information

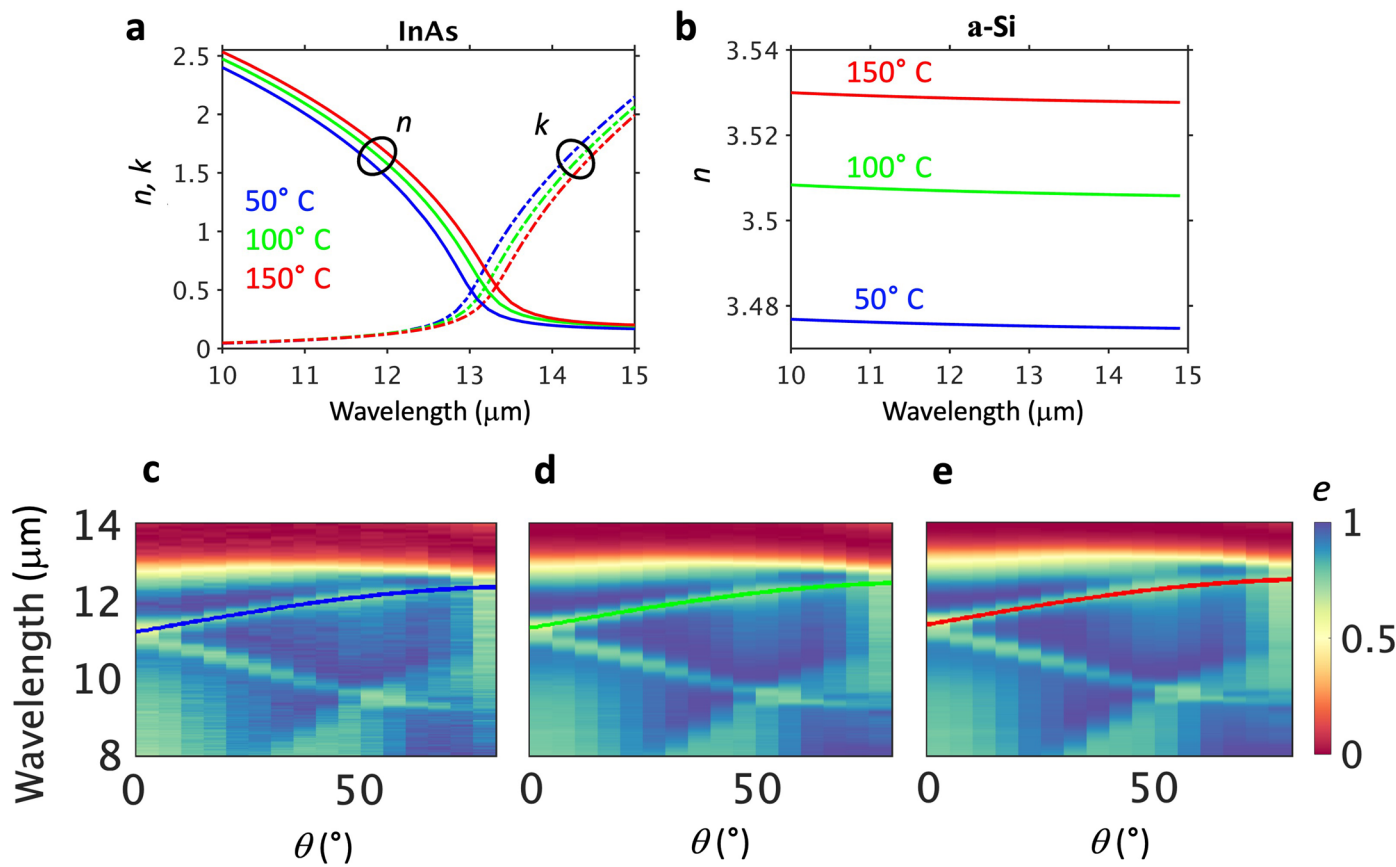
**Extended data** is available for this paper at <https://doi.org/10.1038/s41566-023-01261-6>.

**Supplementary information** The online version contains supplementary material available at <https://doi.org/10.1038/s41566-023-01261-6>.

**Correspondence and requests for materials** should be addressed to Harry A. Atwater.

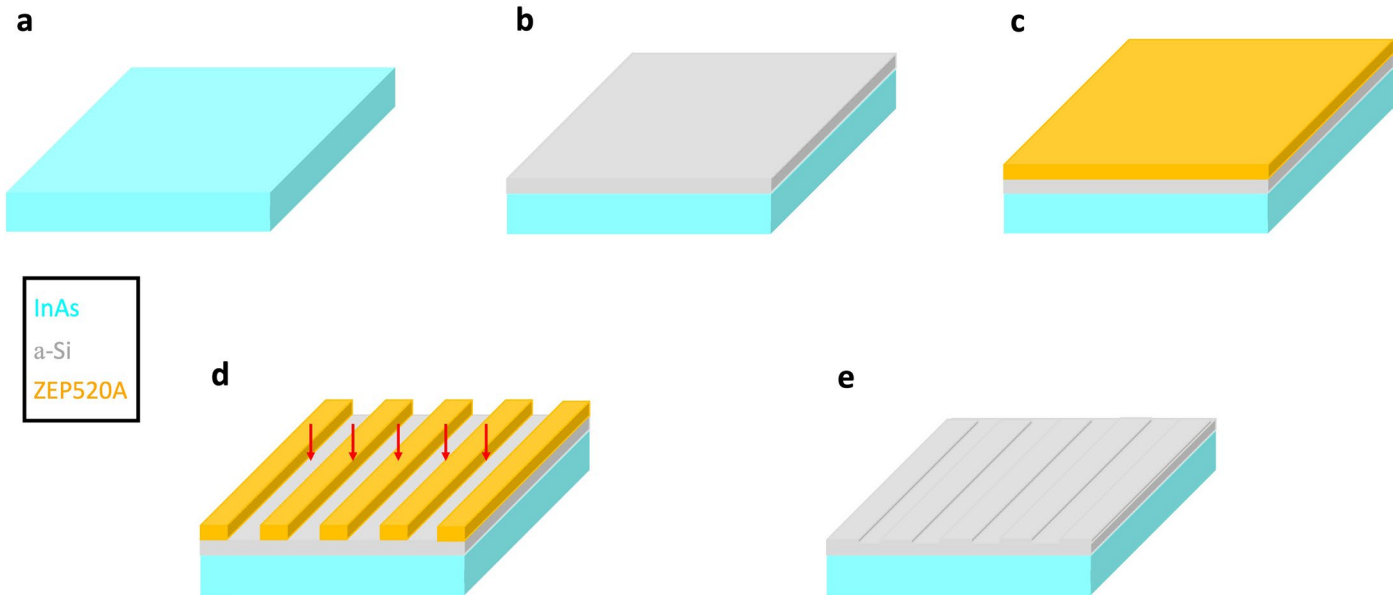
**Peer review information** *Nature Photonics* thanks Denis Baranov and the other, anonymous, reviewer(s) for their contribution to the peer review of this work.

**Reprints and permissions information** is available at [www.nature.com/reprints](http://www.nature.com/reprints).



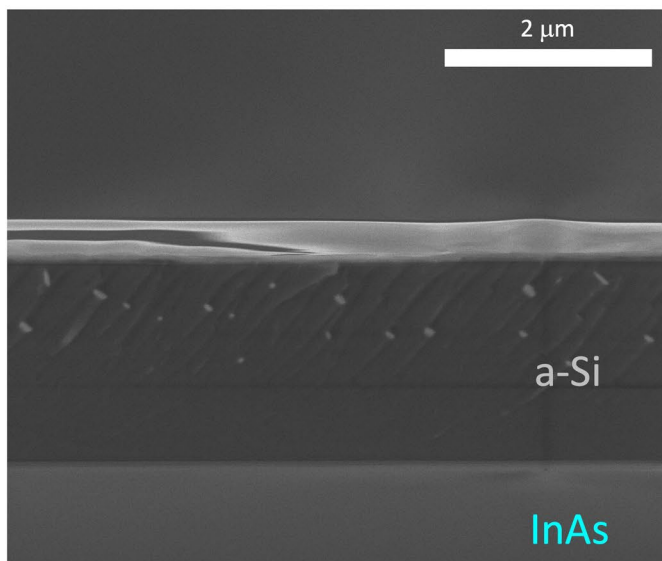
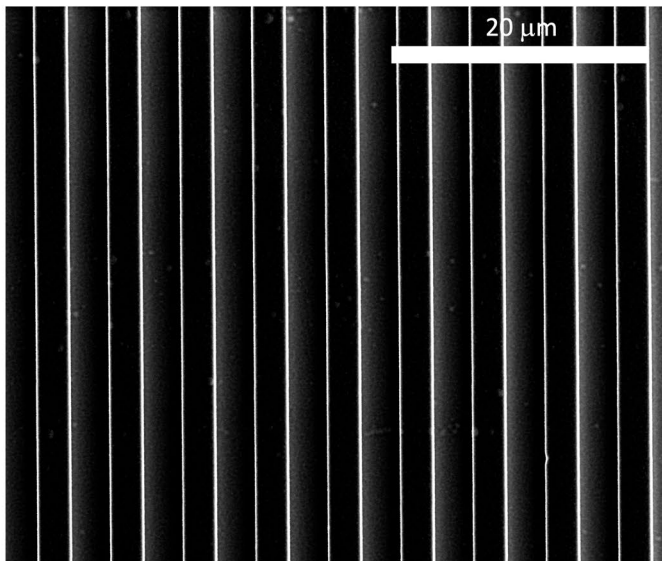
**Extended Data Fig. 1 | Refractive indices of InAs and a-Si and heated emissivity measurements.** (a) Refractive index values ( $n$  and  $k$ , solid and dot-dashed lines respectively) of the InAs wafer for various temperatures. We observe shifts in  $n$  and  $k$  that correspond to a redshifting of the ENZ-wavelength of the wafer. (b) Temperature-dependent refractive index values of the deposited a-Si. The refractive index grows as a function of temperature.

The extinction coefficient is negligible in the wavelength range. (c–e) Emissivity measurements taken at 50, 100, and 150 °C, respectively. The blue, green, and red curves are obtained by solving E.E.D. 1 using the average measured refractive index of a-Si at each temperature. Both (a) and (b) were measured and fitted using a J.A. Woollam IR-VASE and the WVASE software.

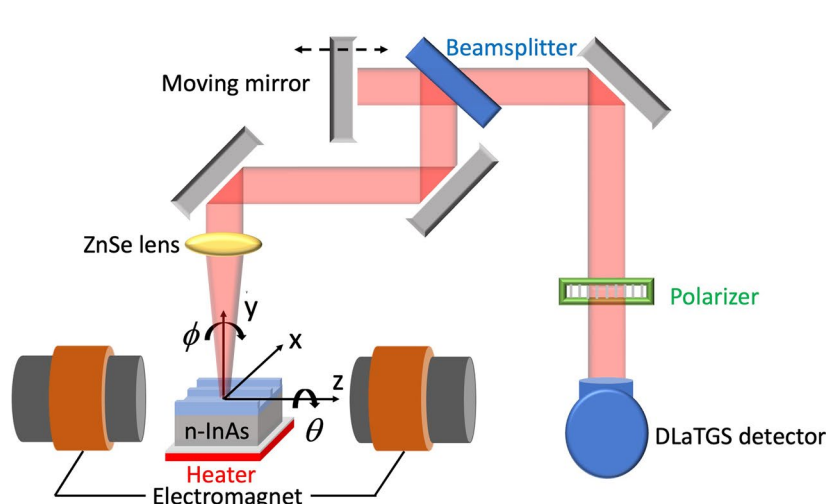
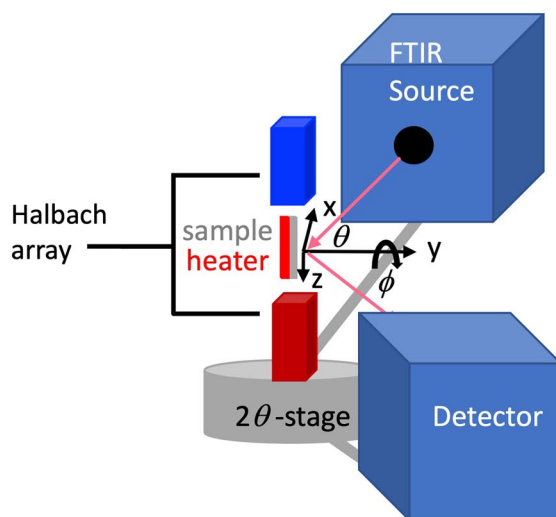


**Extended Data Fig. 2 | Fabrication process of sample.** (a) We begin with a bare InAs wafer for which we have already determined the temperature-dependent optical properties. (b) a 2- $\mu\text{m}$ -thick a-Si layer is deposited on top of the InAs wafer via PECVD. (c) A 750-nm-thick layer of resist, ZEP520A, is spun onto the wafer and the grating pattern is written into the resist via EPG. (d) The pattern

is then developed, and remaining resist is baked. The resist left on the sample surface acts as a mask for the ICP-RIE process. (e) The resist mask is removed overnight and the a-Si GMR structure is cleaned and imaged with an optical microscope and SEM.

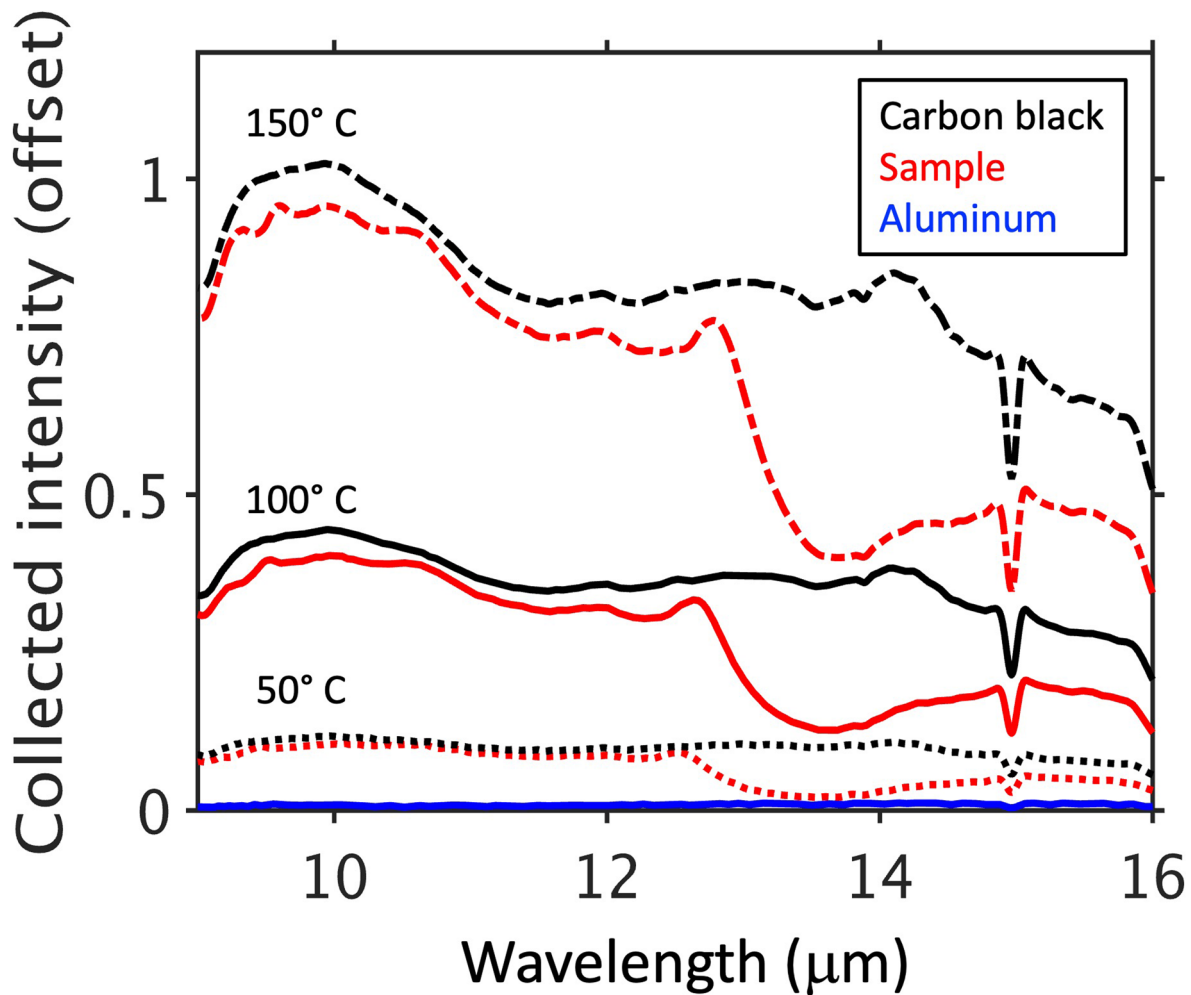
**a****b**

**Extended Data Fig. 3 | SEM images of a-Si layer and grating structure.** (a) Side-view SEM image of the 2-μm-thick a-Si layer on top of the InAs wafer. This sample was not used for the final grating structure, but rather for the optical characterization of the a-Si layer. (b) Top-view SEM of the fabricated grating structure.

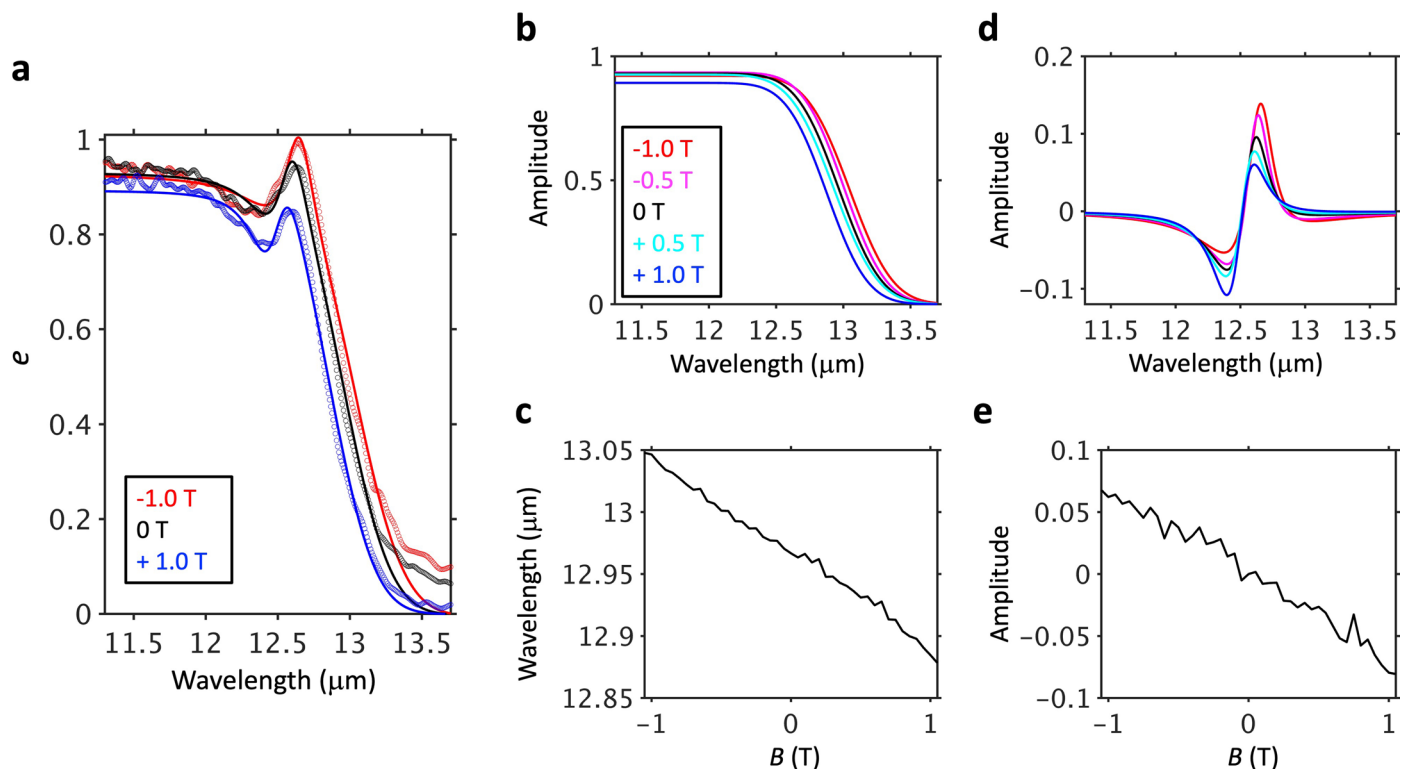
**a****b****Extended Data Fig. 4 | Schematics of the emissivity and absorptivity**

**measurement setups.** (a) For emissivity measurements, the sample is mounted on a heater at the rotation axis of a goniometer, centered between the pole pieces of an electromagnet. The goniometer allows us to rotate the sample around the z-axis and probe the outgoing radiation at an angle  $\theta$ . The sample emission is collected through a ZnSe lens and sent through an external port into an FTIR. We place a polarizer in front of the detector to resolve the TM and TE emission.

(b) The absorptivity measurement system uses an FTIR source and detector mounted on a 2-θ rotation stage. Instead of an electromagnet, we use a Halbach array of permanent magnets to apply the magnetic field. The sample is still heated to the same temperatures as in the emissivity measurements so that we have a direct comparison of the absorptivity and emissivity as defined by the Kirchhoff's Law.

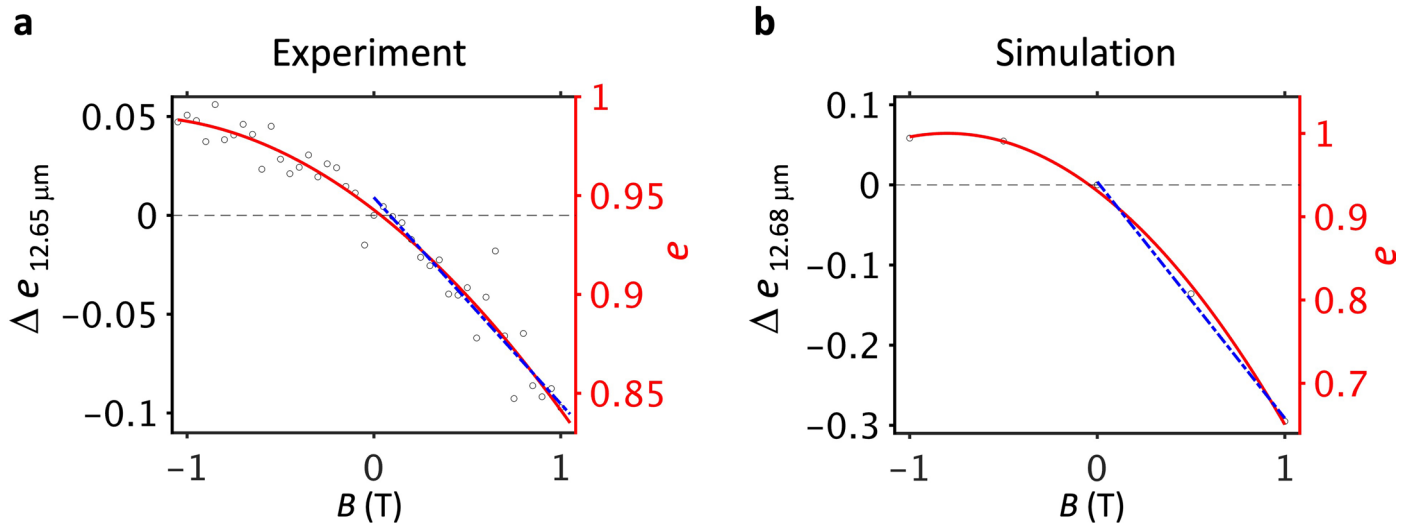


**Extended Data Fig. 5 | Normalization of the emissivity data for  $\theta = 65^\circ$ .** Raw traces of the collected emission from a Carbon black reference (black) and the sample (red) at three different temperatures. The blue trace is the emission of Aluminum at 24 °C and represents the background emission contributions from the system. Traces taken at different temperatures are offset for clarity.



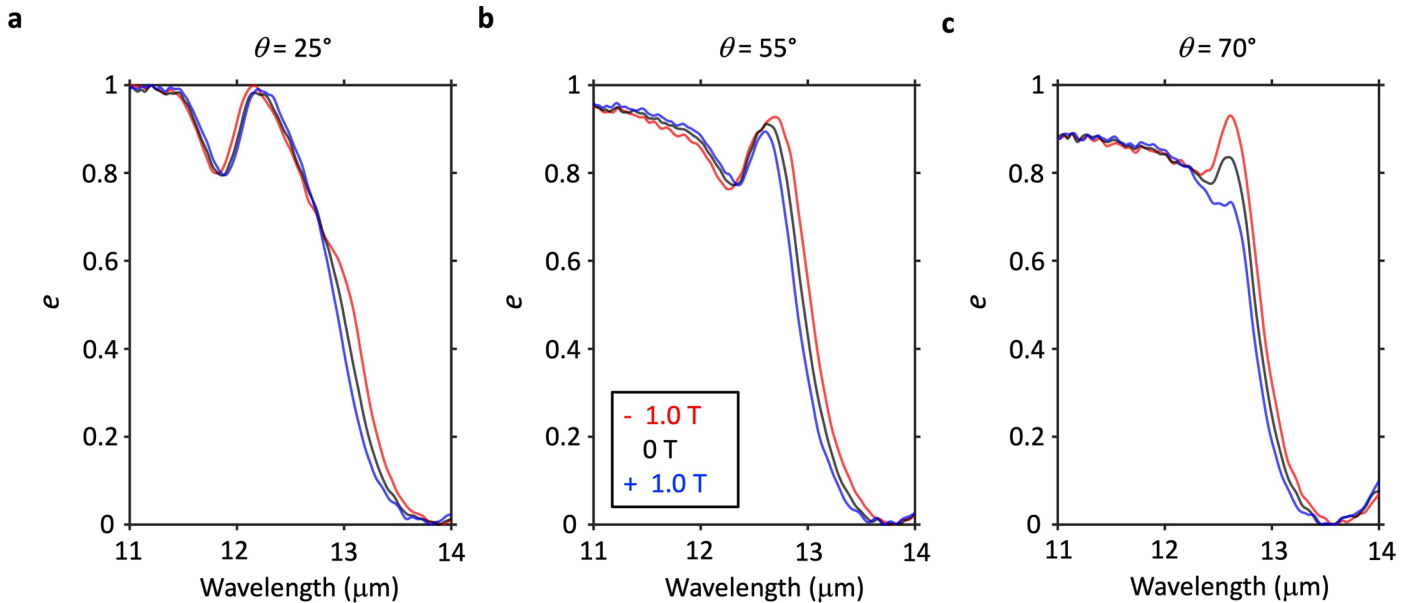
**Extended Data Fig. 6 | Fitting results from the fine magnetic field sweep at  $\theta = 65^\circ$ .** (a) Experimental data and fits for three different magnetic fields. (b) The extracted InAs contribution to the emissivity (amplitude) for varying magnetic field, modeled as a sigmoid. (c) Central wavelength of the InAs contribution (that is the sigmoid) for varying magnetic field. We observe a blueshift of the emission

edge with increasing magnetic field. (d) The resonant emissivity contribution (amplitude) of the GMR structure is modified, but the spectral shift is dictated by the InAs magnetic field response (b and c). (e) Change in the resonant amplitude for all magnetic field values.



**Extended Data Fig. 7 | Experimental and simulated emissivity change for non-zero magnetic field exhibiting saturation effect as resonant sample emissivity approaches Blackbody limit. (a)** Experimental data (black points) with quadratic fit (solid red) for the full magnetic field range and linear fit (dot-dash blue) for the positive magnetic field range. **(b)** The same plot as in (a) for

our simulated photonic structure. The magnitude of the change in emissivity as a function of magnetic field is larger, however we observe the same saturation behavior. Note that our resonant peak emissivity at  $\theta = 65^\circ$  is at a slightly longer wavelength ( $\lambda = 12.68 \mu\text{m}$ ).



**Extended Data Fig. 8 | Experimental data comparing different regimes of the spectral and amplitude tuning of the peak emissivity for three angles.** (a) Emissivity for  $\theta = 25^\circ$  for three magnetic field values. At small angles, the spectral overlap of the InAs emissivity edge ( $\sim 13 \mu\text{m}$ ) and the  $+1^{\text{st}}$  order GMR ( $\sim 12.1 \mu\text{m}$ ) is minimal, resulting in no tuning of the spectral position or magnitude of the emissivity peak of the overall structure. (b) At  $\theta = 55^\circ$ , the

spectral position of the emissivity peak is tuned by the direction of the InAs emissivity edge shift (blueshift for  $+1.0 \text{ T}$  and redshift for  $-1.0 \text{ T}$ ) relative to the  $+1^{\text{st}}$  order GMR. We term this angular range where the InAs emissivity edge begins to change the spectral position of the emissivity peak as the ‘critical angle’  $\theta_c$ . (c) For large angles, we get strong emissivity amplitude tuning with little shift in the spectral position of the resonant emissivity.

# Direct observation of the violation of Kirchhoff's law of thermal radiation

---

In the format provided by the  
authors and unedited

# **Direct Observation of Kirchhoff Thermal Radiation Law Violation**

## **Supplementary Information**

### **Table of Contents**

---

- I. Simulations
- II. Conical diffraction mounting of sample

## I. Simulations

To simulate the response of our photonic structure, we use the COMSOL Multiphysics electromagnetic waves package in the frequency domain. In our simulations, we used the elevated-temperature refractive index values of the *n*-InAs and *a*-Si to get an estimate of the response of the structure in the mid-infrared. For zero magnetic field, Kirchhoff's law dictates that our sample emissivity and absorptivity are equal. When we apply the transverse magnetic field, the simulations (in agreement with our experiment) of  $\alpha(\theta, B)$  equate to  $e(\theta, -B)$ . Both the TM and TE modes supported by the fabricated photonic structure are captured by our simulations (Fig. S1). There is a slight redshift of the modes in simulations that we attribute to slightly smaller periodicity ( $\Lambda \cong 5.45 \mu\text{m}$ ) of the fabricated and experimentally measured photonic structure (Extended Data Fig. 3 b).

Before switching the magnetic field on, however, we examine the guided mode resonant and non-resonant response of our structure. Looking at normal incidence ( $\theta = 0^\circ$ ), we get a clear notch in the absorptivity at  $11.6 \mu\text{m}$  (Fig. S2 a) that correlates with the central wavelength,  $\lambda_c$ , (resonance condition at  $\theta = 0^\circ$ ) of the guided mode. As we increase the angle of incidence, the guided mode splits into the +1<sup>st</sup> and -1<sup>st</sup> (longer and shorter wavelengths respectively) order branches. As an example, we plot the simulated absorptivity spectrum for  $\theta = 65^\circ$ . We no longer have resonant conditions at  $11.6 \mu\text{m}$  (Figs. S2 a, c), but two resonances at  $10.4 \mu\text{m}$  and  $12.7 \mu\text{m}$ .

We visualize the change in emissivity at given angles by subtracting the positive magnetic field spectra from the negative field spectra. Plotting the difference for the same incidence angles we measured, we can qualitatively compare the changes in emissivity as a function of field for our simulations and the experiment. Despite a factor of two difference, we observe the same general features and behavior of the structure emissivity under applied transverse magnetic field (Fig. S2). In Figs. S3 a and c, we see the intersection of the *n*-InAs Brewster mode with the +1<sup>st</sup> order guided mode of the dielectric grating ( $\theta = 65^\circ$ ) (1). Taking linecuts of the difference across a narrow spectral band encompassing the Brewster and GMR for the simulation and experiment, we observe that the average change in the emissivity is larger for larger angles, because of the larger spectral overlap of the GMR with the InAs Brewster mode.

## II. Conical diffraction mounting of sample

We also look at other orientations of the photonic structure, namely different azimuthal orientations of the grating ( $\phi \neq 0^\circ$ ), in an external magnetic field (Figs. S4 a and b). This is of particular interest for future work that aims to remove the use of a magnetic field in favor of a gyrotrropic optical response stemming from topological electronic structure (e.g. a magnetic Weyl semimetal) (2, 3, 4). In such a system, the time-reversal-symmetry-breaking field would be fixed relative to any external patterning or structure.

The optical response of our system for  $\phi \neq 0^\circ$  is also known as the conical diffraction mounting. In Fig. S4, we show the change in the spectral directional emissivity and absorptivity for different  $\phi$ . As we rotate the grating, we still excite the fundamental guided mode for  $\phi = 0^\circ$ ,

albeit less efficiently (Figs. S4 b, e, h). At  $\phi$  approaching  $90^\circ$ , the modes excited in the *a*-Si layer follow the same general angular dependence as the InAs Brewster modes. Again, we are able to match the directional spectral absorptivity and emissivity over  $35^\circ < \theta < 80^\circ$  (Figs. S4 d-i).

Performing the same operation as in Fig. 2 a of the main text, we can see that the effect of rotating the sample and magnetic field azimuthally reduces the emissivity change as a function of field (Fig. S5). This reduction is not surprising given that the structure was optimized for  $\phi = 0^\circ$ , however it is worth noting that there is still a non-negligible magnetic field effect for  $\phi = 90^\circ$ . This means that despite complete misalignment of the grating, there is still coupling between the slab waveguide modes supported by the *a*-Si layer and the InAs. In fact, the effect of the magnetic field on the structure emissivity tuning is only reduced by a factor of two when rotated from  $\phi = 0^\circ$  to  $\phi = 90^\circ$ .

Beyond rotating the sample azimuthally, we also applied the magnetic field in the longitudinal direction, i.e., along x-axis, or Faraday configuration. We observed no shift in the absorptivity for either the  $\phi = 0^\circ$  or  $\phi = 90^\circ$  orientations for both the TM and TE modes as a function of magnetic field (Fig. S7). The case of TM modes remaining unchanged is because the cross product of the electric field and external magnetic field equals zero.



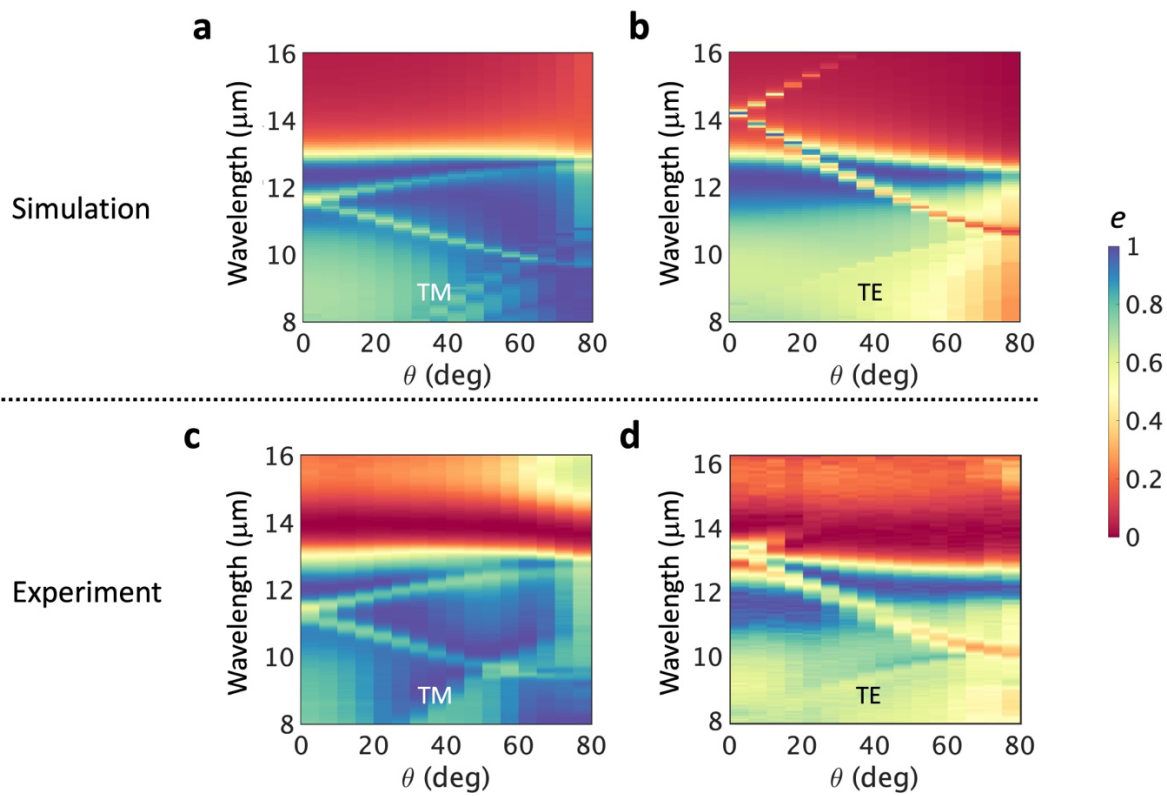


**Fig. S1: Comparison of simulated TM and TE emissivity spectra to experimental measurements of spectral directional emissivity from our photonic structure.** (a) Simulated spectral and angular emissivity intensity for transverse magnetic and (b) transverse electric polarized emission. (c and d) Experimentally measured TM and TE spectral directional emissivity. Both the TM and TE data were taken at 100° C.

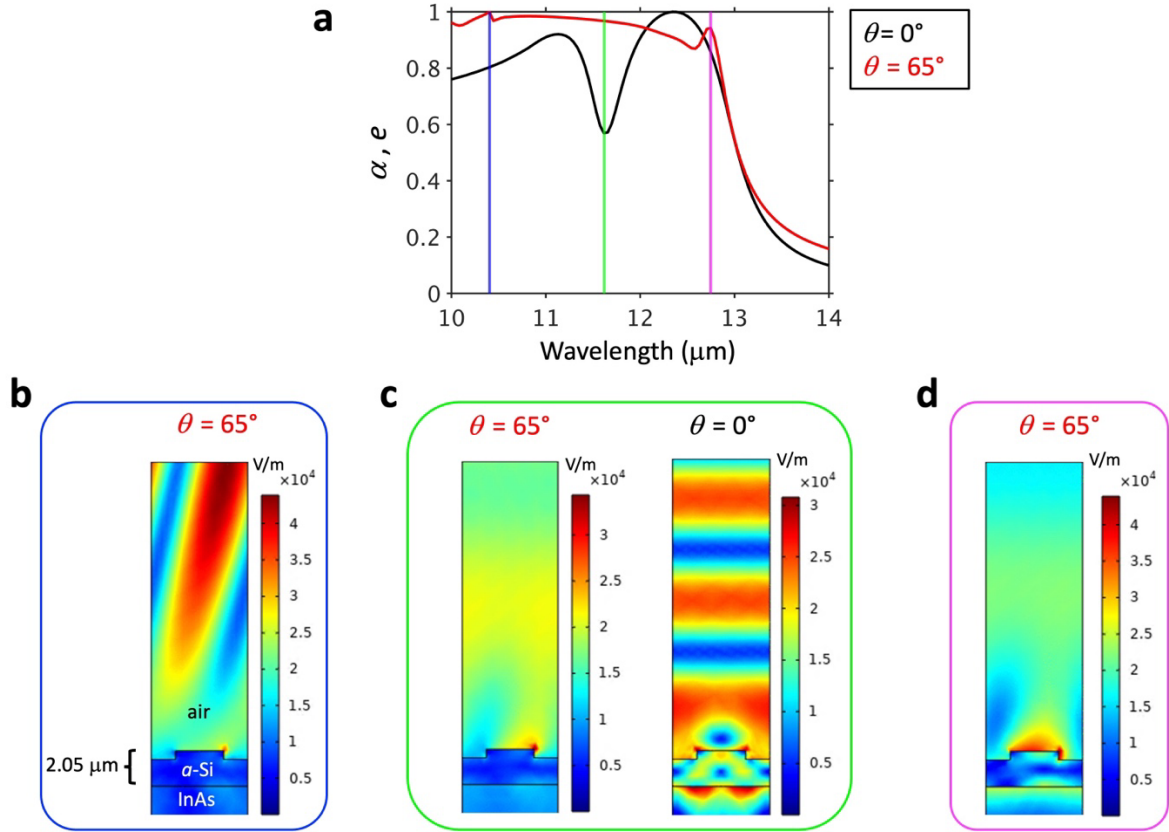


**Fig. S2: Comparison of simulated spectra and electric field intensities for  $\theta = 0^\circ$  and  $65^\circ$ .** (a) Simulated emissivity spectra with lines marking the guided-mode resonances for  $\theta = 0^\circ$  (green) and  $\theta = 65^\circ$  (blue and magenta). (b and d) Electric field intensity plots for the -1<sup>st</sup> and +1<sup>st</sup> guided modes respectively. (c) Comparison of resonant ( $\theta = 0^\circ$ ) and non-resonant ( $\theta = 65^\circ$ ) excitation at the central wavelength,  $\lambda_c = 11.6 \mu\text{m}$ .

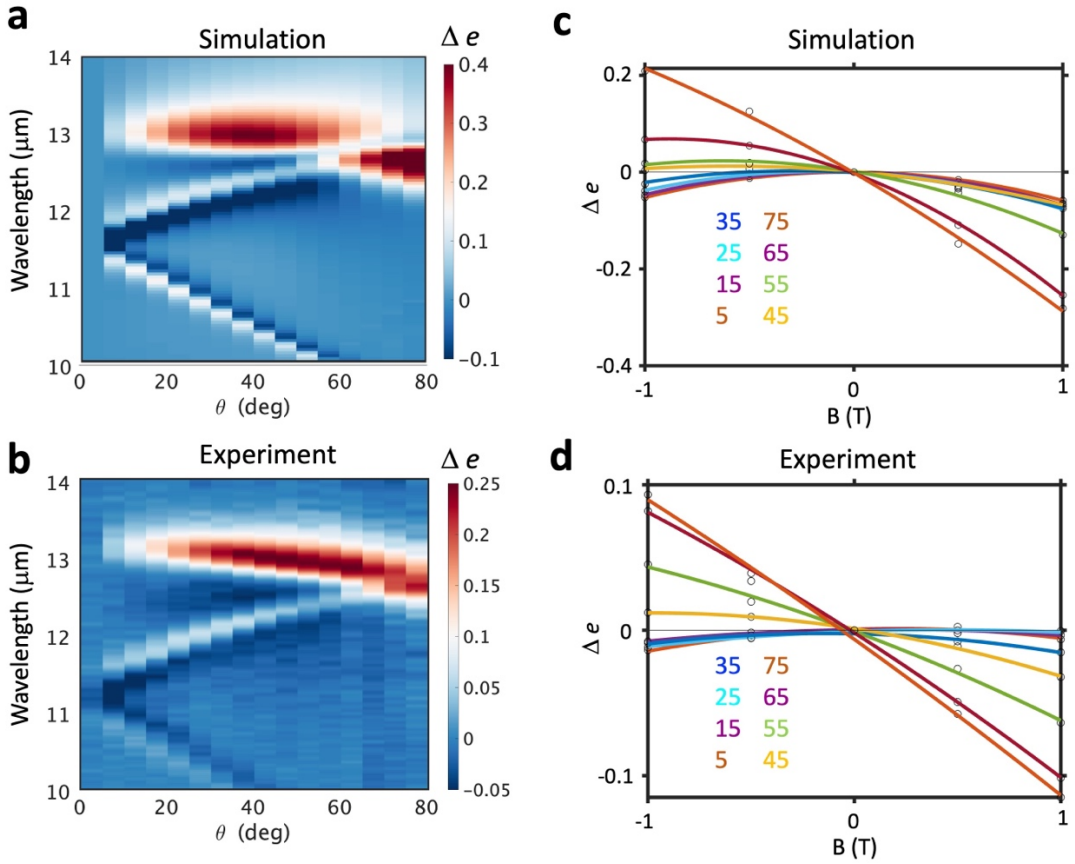


**Fig. S3: Comparison of simulated and experimental data of the change in emissivity for varying magnetic field.** (a) Simulated difference between the +1 T and -1 T emissivity. The intersection of the Brewster mode and the +1<sup>st</sup> order guided mode resonance is visible near  $\theta = 60^\circ$ . (b) The same plot for our experimental data, taken at 100°C. The same intersection occurs at slightly larger angles, with the +1<sup>st</sup> order guided mode being slightly blueshifted compared to the simulations ( $\lambda_c = 11.2 \mu\text{m}$ ). (c and d) Average change in emissivity from 12.5 to 12.8  $\mu\text{m}$  for the simulated and experimental data, respectively, for different angles  $\theta$  as indicated. The average change over this range is quadratic because of the saturation effect, although appears linear for large angles of incidence. This is because at large  $\theta$ , the 12.5 to 12.8  $\mu\text{m}$  range spans the InAs emission edge, which linearly shifts with magnetic field (Fig. S6).

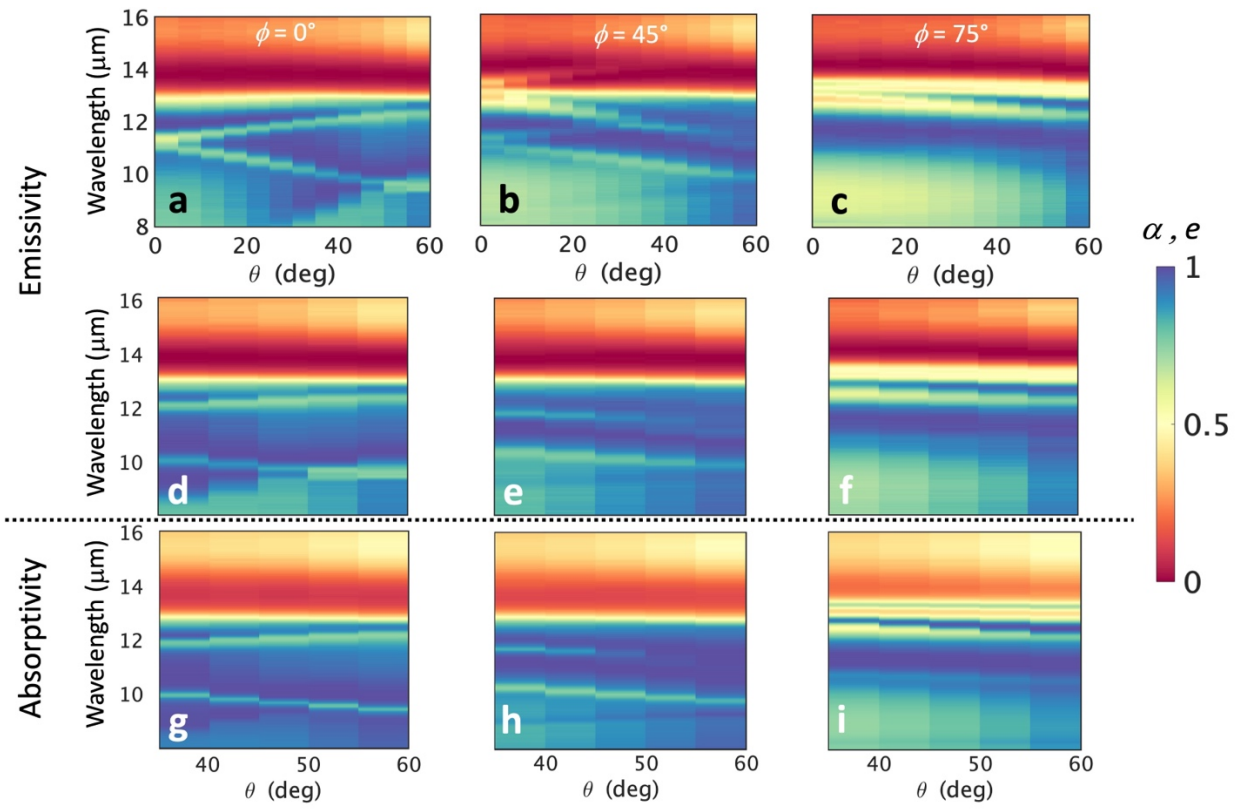


**Fig. S4: Comparison of spectral directional absorptivity and emissivity for varying azimuthal angle ( $\phi$ ).** (a - c) Full angular spectral emissivity data for  $\phi = 0^\circ$ ,  $45^\circ$ , and  $75^\circ$  at 100°C. (a) For  $\phi = 0^\circ$ , the upper and lower guided-mode branches are clearly visible, starting from a central wavelength around  $\lambda_c = 11.2 \mu\text{m}$  at  $\theta = 0^\circ$ . (b) The same modes are visible for  $\phi = 45^\circ$ , however, a longer wavelength mode with  $\lambda_c = 13 \mu\text{m}$  appears. (c) The longer wavelength mode with  $\lambda_c = 13 \mu\text{m}$  narrows spectrally and follows the Brewster mode as we increase the azimuthal angle to  $\phi = 75^\circ$ . The original +1<sup>st</sup> and -1<sup>st</sup> order guided modes for  $\phi = 0^\circ$  are no longer excited. (d - f) Emissivity and (g - i) absorptivity spectral data over the same angular range for comparison.

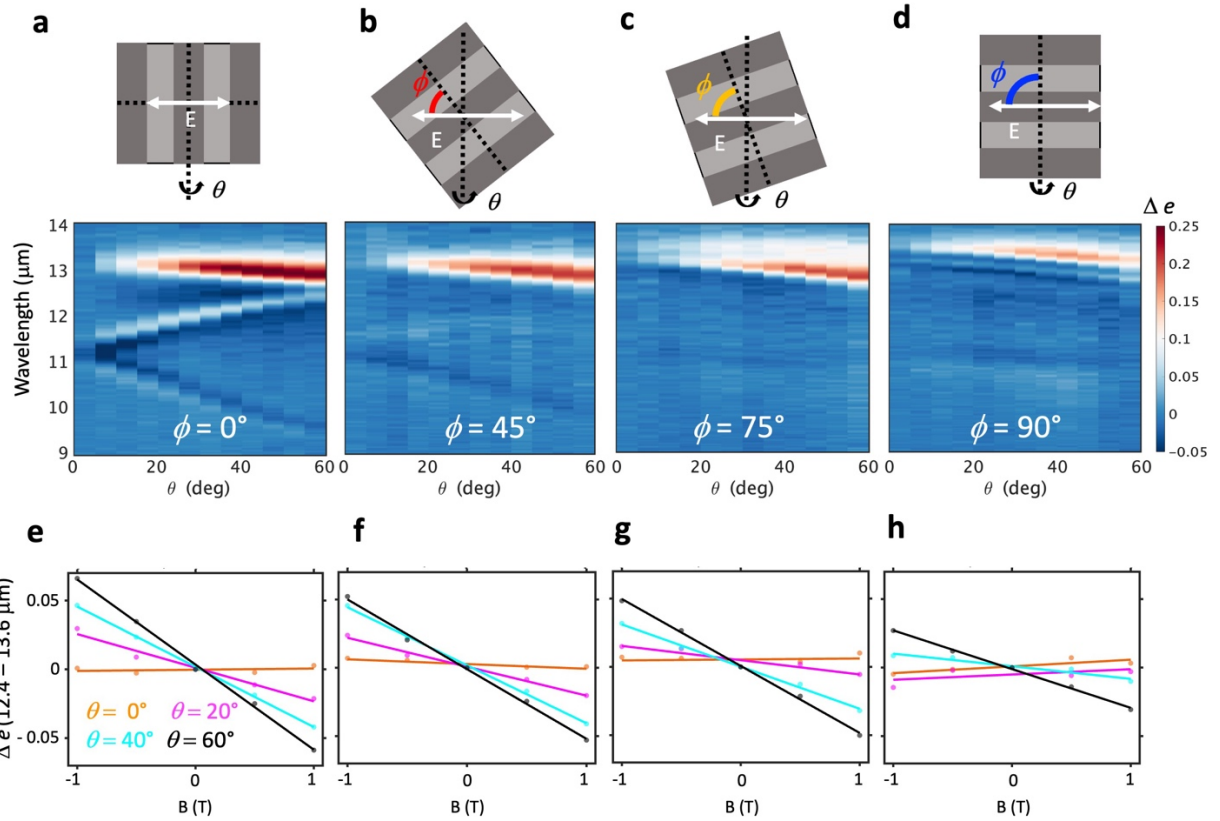


**Fig. S5: Comparison of emissivity tuning for varying azimuthal angle.** (a - d) (Top) Schematic showing the direction of the electric field relative to the grating. (Bottom) Change in emissivity from +1.0 T to -1.0 T for varying azimuthal angles. With larger  $\phi$ , the coupling efficiency between the GMR and the InAs layer decreases, resulting in weaker tuning of emissivity with magnetic field. (e - h) Average change in the emissivity over a large wavelength range (12.4 – 13.6  $\mu\text{m}$ ) as a function of magnetic field for varying angles of incidence.

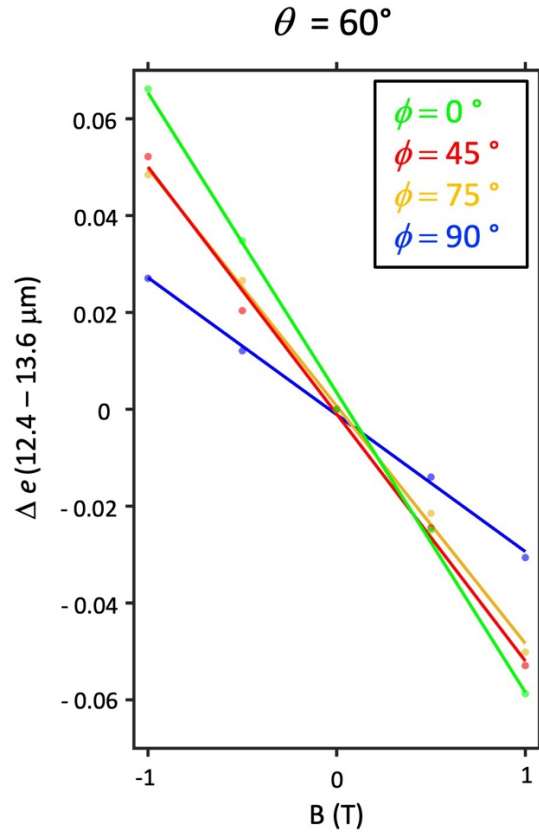


**Fig. S6: Average change in the emissivity at  $\theta = 60^\circ$  as a function of magnetic field for different  $\phi$ .** Changing the grating orientation from  $\phi = 0^\circ$  to  $\phi = 90^\circ$  reduces the amplitude tuning of the emissivity by over a factor of two. Despite the dispersion alignment of the dielectric resonance with the InAs Brewster mode for large  $\phi$ , the mode-coupling efficiency is greatly reduced. This results in a weaker tuning of the emissivity.

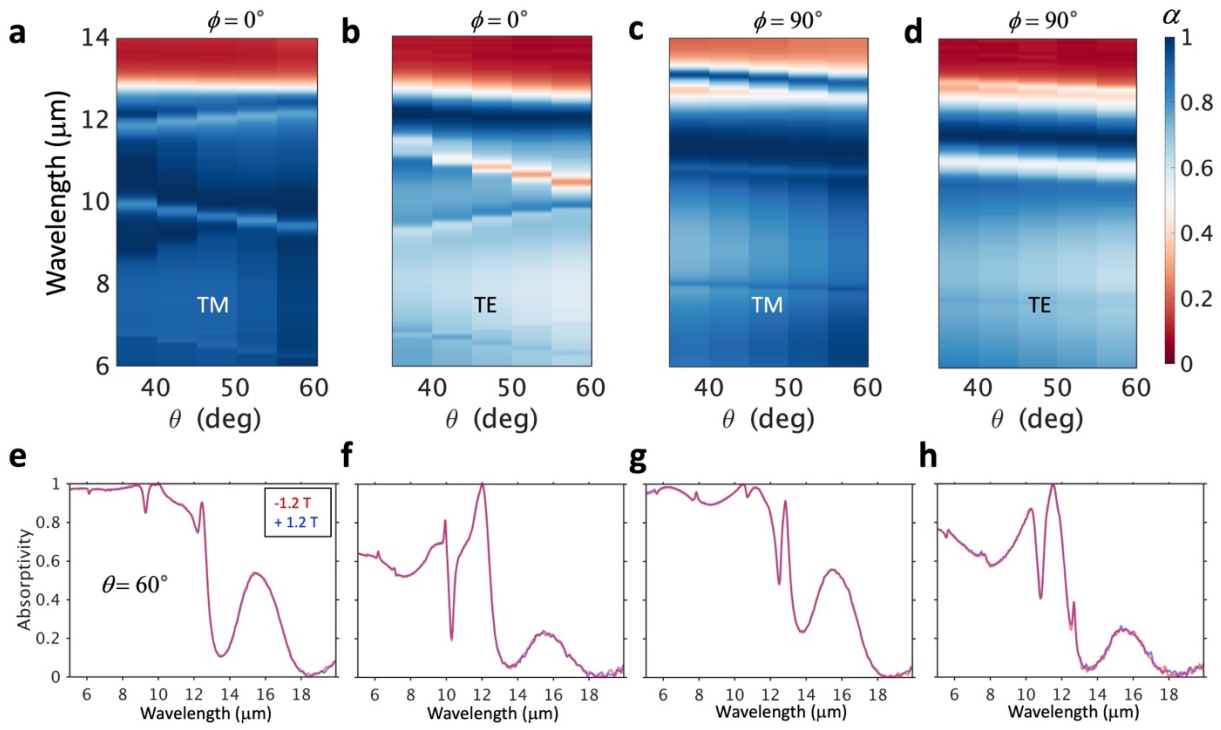


**Fig. S7: Faraday configuration has no effect on absorptivity tuning.** (a – d) Spectral angular absorptivity data for TM- and TE- polarized light for  $\phi = 0^\circ$  and  $\phi = 90^\circ$ . (e – h) Absorptivity spectra for the electric field and azimuthal orientation above (a – d) when a magnetic field is applied along and against the direction of propagation. The Faraday configuration does not have any coupling effect to either the TM or TE absorptivity.

- 
- [1] T. Tallercio, V. N. Guilengui, L. Cerutti, E. Tournié, J. J. Greffet, Brewster “mode” in highly doped semiconductor layers: an all-optical technique to monitor doping concentration. *Optics Express* **22**, 24294-24303 (2014).
  - [2] Y. Okamura, et al., Giant Magneto-optical responses in magnetic Weyl semimetal  $\text{Co}_3\text{Sn}_2\text{S}_2$ . *Nat. Comm.* **11**, 4619 (2020).
  - [3] B. Zhao, C. Guo, C. A. Garcia, P. Narang, S. Fan, Axion-Field-Enabled Nonreciprocal Thermal Raduation in Weyl Semimetals. *Nano Lett.* **20**, 1923-1927 (2020).
  - [4] C. Guo, V. S. Asadchy, B. Zhao, S. Fan. Light control with Weyl semimetals. *arXiv* (2022). 2209.00701.